PERGAMON

Journal of Atmospheric and Solar-Terrestrial Physics 65 (2003) 245–267

Journal of ATMOSPHERIC AND SOLAR-TERRESTRIAL PHYSICS

www.elsevier.com/locate/jastp

Mesospheric temperature from UARS MLS: retrieval and validation

D.L. Wu[a,*], W.G. Read[a], Z. Shippony[a], T. Leblanc[a], T.J. Duck[b], D.A. Ortland[c], R.J. Sica[d], P.S. Argall[d], J. Oberheide[e], A. Hauchecorne[f], P. Keckhut[f], C.Y. She[g], D.A. Krueger[g]

[a] *Jet Propulsion Laboratory, California Institute of Technology, 4800 Oak Grove Drive, Pasadena, CA 9109, USA*
[b] *Department of Physics and Atmospheric Science, Dalhousie University, Halifax, N.S., Canada*
[c] *Northwest Research Associates, Bellevue, Washington, DC, USA*
[d] *Department of Physics and Astronomy, The University of Western Ontario, London, Ont., Canada*
[e] *Physics Department, University of Wuppertal, Wuppertal, Germany*
[f] *Service d'Aeronomie du CNRS, Verrieres-le-Buisson Cedex, France*
[g] *Physics Department, Colorado State University, Fort Collins, CO, USA*

Received 9 April 2002; received in revised form 30 September 2002; accepted 6 November 2002

Abstract

A research algorithm is developed to retrieve temperature at 20–90 km using 63 GHz O_2 emission measurements from Microwave Limb Sounder (MLS) on Upper Atmosphere Research Satellite (UARS). The algorithm is based on a previous MLS radiative transfer model but improved to produce more accurate radiance calculations in the cases where the geomagnetic Zeeman splitting is important. A fast version of the model is developed and implemented for practical uses of the temperature retrieval, which uses a single temperature and O_2 density profile as the linearization basis. The calculated radiances and linearization coefficients are fit to a set of explicit functions of the geomagnetic field and its direction at tangent heights of 0–120 km, which are pre-stored in order to speed up the computation. The new algorithm has been used to process all the data available during 1991–1997 before MLS 63 GHz radiometer was powered off. The estimated precision of MLS temperature varies from 2 K at ~20 km to 8 K at ~80 km and increases sharply above ~90 km. The retrieved MLS temperature are compared against CIRA'86, satellite, lidar, and rocket observations. Comparisons to CIRA'86 seasonal climatology show that the differences are latitude-and-season dependent and generally < 5 K below 50 km and 10 K in the mesosphere. Comparisons with other satellite observations (ISAMS, HRDI, CRISTA1) show different patterns but a cold bias at 85–90 km seems common in all these comparisons. Comparisons to ground-based lidar measurements suggest that MLS temperatures are warmer by 2–4 K in the stratosphere and colder by 5–15 K at 85–90 km. The MLS-minus-lidar difference shows a 3–10 K cold bias near 70 km for most of the sites selected. The comparisons with rocket measurements are similar to those with lidars at these altitudes, giving cold biases in the MLS temperatures at 85–90 km. Most of these biases are understandable in terms of sampling and resolution differences, and some biases can be reduced with further improvements in the MLS retrieval algorithm. Despite the existing biases, the MLS temperature have been found useful in studying large-scale mesospheric phenomena such as the temperature inversion layer.
© 2002 Elsevier Science Ltd. All rights reserved.

Keywords: Mesospheric temperature; Pressure; Microwave observation; Zeeman effect; Satellite remote sensing

* Corresponding author. Fax: +818-393-5065.
E-mail address: dwu@mls.jpl.nasa.gov (D.L. Wu).

1364-6826/03/$ - see front matter © 2002 Elsevier Science Ltd. All rights reserved.
doi:10.1016/S1364-6826(02)00293-6

1. Introduction

Understanding upper-atmospheric variability requires accurate measurements of temperature and density profiles. Global observations of these variables in the mesosphere remain sparse due to limitations with remote sensing techniques. Satellite measurements of mesospheric temperature in the past are provided mainly from infrared [e.g., the Solar Mesosphere Explorer (SME), the Limb Infrared Monitor of the Stratosphere (LIMS), the Improved Stratospheric and Mesospheric Sounder (ISAMS)] and visible [e.g., the High Resolution Doppler Imager (HRDI)] techniques. Rockets and lidars are the primary means to obtain high-resolution mesospheric temperature profiles on a long-term basis but the number of observing locations are limited.

Passive microwave radiometers have advantages of measuring mesospheric temperature with O_2 thermal emissions. One of the advantages is the validity of local thermodynamic equilibrium (LTE) approximation in the mesosphere, which can be a problem at these altitudes for infrared techniques. However, the microwave techniques using O_2 emission features need to deal with the Zeeman splitting problem due to the geomagnetic field. Observations have shown that the Zeeman splitting effect becomes significant for radiances within a few MHz of the line center (Waters, 1973; Hartmann et al., 1996). Substantial progresses have been made in the past three decades to provide accurate modeling of the Zeeman split O_2 radiances in the mesosphere (Lenoir, 1968; Rosenkranz and Staelin, 1988; Liebe, 1989; Pardo, 1995).

Stogryn (1989a, b) proposed a useful algorithm to retrieve temperature up to ~70 km from the nadir-viewing Advanced Microwave Sounding Unit-A (AMSU-A) 57–63 GHz measurements. von Engeln et al. (1998) were able to retrieve temperature at 30–90 km from the O_2 radiances near 63 GHz (9+, 15+, 17+) measured by the limb-viewing Millimeter-Wave Atmospheric Sounder (MAS) on space shuttles during Atmospheric Laboratory for Applications and Science (ATLAS) missions in 1992–1994. Since these retrievals are often time consuming in forward model calculations, Stogryn (1989a) suggested to use a fast model in which the model radiances are expended on a set of basis functions related to the geomagnetic field. Such pre-calculated radiance model can be run as fast as near operationally.

In this paper we develop a research algorithm that is fast enough to retrieve 6 years of temperature at 20–90 km from the O_2 63 GHz radiance measurements with Upper Atmosphere Research Satellite (UARS) Microwave Limb Sounder (MLS). We adopt the similar approach suggested by Stogryn (1989a) to form the fast forward model that has sufficient accuracy for the MLS radiances and weighting functions at each tangent pressure, temperature, and O_2 mixing ratio under all the geomagnetic conditions UARS MLS may encounter. In the early versions of MLS temperature retrieval, such radiative transfer calculations were insufficient to handle all the Zeeman splitting cases due to the geomagnetic field, yielding useful temperatures only at 20–55 km (Fishbein et al., 1996; Livesey et al., 2002). With this improved algorithm, we are able to retrieve temperature up to ~90 km. Comparisons of the new MLS temperature to lidar, rocket and other satellite measurements can be found in the end of this paper.

Table 1
Channel parameters of MLS 63 GHz radiometer

Channel	Center frequency (MHz)	3 dB-bandwidth (MHz)	Calibrated random noise (K)	Sideband ratio (r_u/r_l)
1	181.63	118.86	0.029	1.13
2	92.56	64.57	0.037	1.00
3	46.51	31.75	0.052	1.13
4	22.69	15.76	0.074	1.21
5	10.92	8.03	0.10	1.25
6	4.89	3.82	0.15	1.27
7	1.93	1.92	0.21	1.28
8	0.00	2.00	0.22	1.28
9	−1.95	2.07	0.20	1.29
10	−5.27	3.69	0.15	1.30
11	−10.94	7.65	0.12	1.31
12	−23.40	15.59	0.074	1.36
13	−48.01	31.90	0.050	1.44
14	−92.63	62.36	0.034	1.08
15	−161.28	63.56	0.032	0.43

2. UARS MLS experiment

Launched in September 1991, the UARS MLS is a passive instrument with three radiometers to measure stratospheric ClO, O_3, H_2O, and temperature and constituents using emission features near 63, 183, and 205 GHz (Waters, 1993; Barath et al., 1993). The MLS 63 GHz radiometer contains a heterodyne receiver with local oscillator frequency at 63.283 GHz such that two O_2 lines (62.988 and 63.569 GHz) are folded at the line centers in the double sideband system. The upper/lower sideband ratios (i.e., r_u/r_l) used in the algorithm can be found in Table 1, which have been adjusted from the manufacture's values to minimize systematic error in MLS radiance measurements (Jarnot et al., 1996; Fishbein et al., 1996). Radiance signals received by the receiver are downconverted with the Schottky-diode mixer to an intermediate frequency (IF) filter bank (of ~500 MHz bandwidth) where they are sampled with 15 spectral channels. The center channel of the filter bank (channel 8) is placed at the line center and channels 1 and 15 measure the wings of the lines. Generally speaking, the channels closer to the line center provide temperature sensitivity at higher altitudes whereas the wing channels have better sensitivity at low altitudes. The channel center

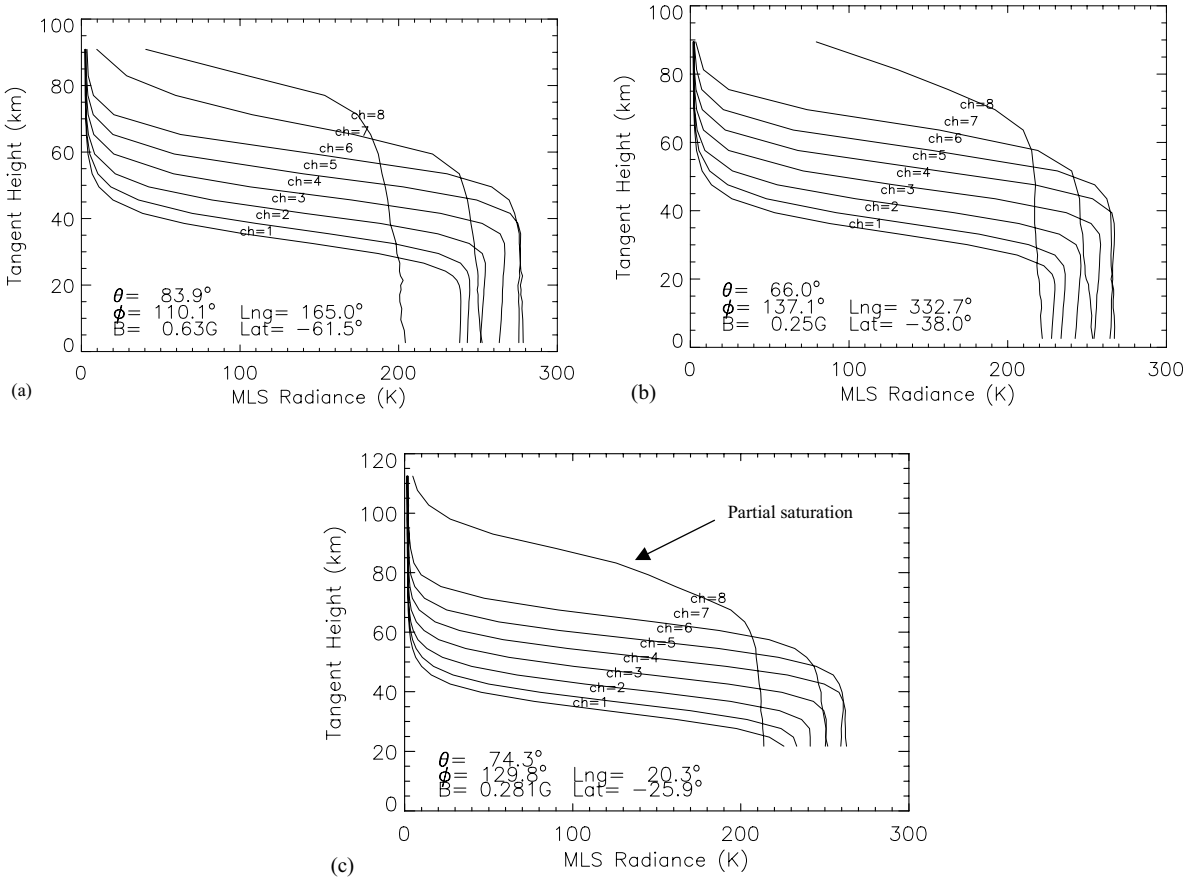

Fig. 1. Examples of MLS 63 GHz radiance profiles for: (a) strong, (b) weak geomagnetic field situations from the normal (0–90 km) scans on January 16, 1992, and (c) weak geomagnetic field case from a special (20–120 km) scan on September 20, 1991. In the cases of weak fields, the ch.8 radiance can be partially saturated as the spectral lines are split only slightly (due to the little Zeeman effect) and occupy a bandwidth narrower than the filter width (2 MHz).

frequencies (relative to the line center), as listed in Table 1, are unevenly spaced to cover a large dynamical range of the pressure-broaden line. The ability to resolve the line width is important in the limb viewing technique since the retrievals of tangent pressure and temperature are coupled. In the mesosphere, the line width becomes very small and most of the information comes from channels 7–9.

MLS field of view (FOV) is essentially determined by the antenna diameter. The measured antenna pattern is used in the forward model, which has a shape like the Gaussian function for the main lobe. The FOV electric field vector of the 63 GHz receiver is 114° from the vertical plane and makes the MLS radiometer close to the horizontal linear polarization. The antenna half-power beamwidth is approximately 9.6 km in the vertical plane at 50 km tangent height.

In normal operation MLS step-scans the atmospheric limb from ~90 km to the surface in 65.5 s with 2 s integration for each measurement. The tangent height interval varies from ~3 km in the stratosphere to ~5 km in the mesosphere. In-flight radiometric calibration is performed for each limb scan with three space views and one ambient target view (Jarnot et al., 1996). Because the instrument views 90° from the UARS moving direction on a 585 km-high and 57°-inclination orbit, MLS latitude coverage is biased on a given day between 34° in one hemisphere to 80° in the other. The satellite performs the 180°-yaw maneuver 10 times a year, which yields alternate views of high latitudes about every 36 days.

Shown in Fig. 1 are the radiance profiles measured by channels 1–8 of the 63 GHz radiometer in strong and weak geomagnetic field cases. Radiance profiles from channels 9–15 are not shown in Fig. 1 because of their similarity to channels 7–1. The measured O_2 lines are split into dozens of lines over 1–2 MHz about the line center under normal geomagnetic conditions ($B = 0.22$–0.65 G). Due to the wide (~2 MHz) bandwidths of MLS center channels, channels 7–9 cannot resolve each individual Zeeman line but they are

sensitive to the width of the Zeeman splitting. This sensitivity is clearly evident in Fig. 1(a) and (b) at high tangent heights (>80 km) with an anti-correlation between ch.7 and ch.8 radiances. In the case of a narrow Zeeman splitting, or the weak geomagnetic field [Fig. 1(b)], stronger radiance is found in channel 8 and weaker radiances are in channel 7 (or channel 9 on the other side of the line center). In the case of a wide splitting, or the strong geomagnetic field [Fig. 1(a)], weaker radiance is found in channel 8 and stronger radiances are in channel 7 (or channel 9). In the case of weak splitting, all the Zeeman lines are clustered in a narrow bandwidth and a partial saturation can happen to channel 8 radiances that have a bandwidth of 2 MHz. At tangent heights above ~80 km, the line widths are close to the Doppler width (~0.07 MHz) with little pressure broadening. The clustered radiation can become saturated over the narrow bandwidth, which is only part of the 2 MHz filter bandwidth, while the radiation in other parts of the filter remains unsaturated. Thus, channel 8 radiances can be a mixture of some saturated and unsaturated radiances, which are often seen in MLS measurements [Fig. 1(c)]. It generally requires much more computing power to accurately model channel 8 radiances than other channels. The effects of the geomagnetic magnetic field on channels 1–6 and 10–15 are much weaker once they are out of the range of the Zeeman splitting.

3. Forward model

3.1. Radiative transfer equation

The brightness temperature $T^{\mathrm{A}}_{\mathrm{b}\|}(v,h_{\mathrm{t}})$, as observed by MLS at frequency v and tangent height h_{t}, is a double-sideband radiance in temperature unit and has been convolved with the FOV and spectral filter functions, namely

$$T^{\mathrm{A}}_{\mathrm{b}\|}(v,h_{\mathrm{t}}) = r_{\mathrm{u}}\int_{\nu_{\mathrm{lo}}}^{\infty}\int_{\Omega_{\mathrm{A}}} T_{\mathrm{b}\|}\,\Phi(v-v')\Psi(\Omega',h_{\mathrm{t}})\,\mathrm{d}\Omega'\,\mathrm{d}v' + r_{\mathrm{l}}\int_{-\infty}^{\nu_{\mathrm{lo}}}\int_{\Omega_{\mathrm{A}}} T_{\mathrm{b}\|}\,\Phi(v-v')\Psi(\Omega',h_{\mathrm{t}})\,\mathrm{d}\Omega'\,\mathrm{d}v', \quad (1)$$

where $r_{\mathrm{u}}/r_{\mathrm{l}}$ is sideband ratio ($r_{\mathrm{u}}+r_{\mathrm{l}}=1$), ν_{lo} is local oscillator frequency, $\Phi(v)$ and $\Psi(\Omega)$ are, respectively, the normalized MLS filter and FOV functions, Ω_{A} is the domain of the FOV functions provided from calibration. In the presence of the geomagnetic field, $T_{\mathrm{b}\|}$ needs to be solved as a part of polarized radiation equation. Lenoir (1967) developed a polarized radiative transfer equation for the atmosphere of magnetic field, which is given by

$$\frac{\mathrm{d}\mathbf{T}_{\mathrm{b}}}{\mathrm{d}s} + \mathbf{G}\mathbf{T}_{\mathrm{b}} + \mathbf{T}_{\mathrm{b}}\mathbf{G}^{\dagger} = \hat{T}(\mathbf{G}+\mathbf{G}^{\dagger}), \quad (2)$$

where $\mathbf{T}_{\mathrm{b}}$ is brightness temperature tensor along path s and contains the polarization properties in the following form:

$$\mathbf{T}_{\mathrm{b}} = \begin{bmatrix} T_{\mathrm{b}\|} & T_{\mathrm{b}|} + \mathrm{i}T_{\mathrm{b}\odot} \\ T_{\mathrm{b}|} - \mathrm{i}T_{\mathrm{b}\odot} & T_{\mathrm{b}\perp} \end{bmatrix}$$

$T_{\mathrm{b}\|}$ is the radiation component co-polarized with MLS receiver, $T_{\mathrm{b}\perp}$ is the cross-polarized component, $T_{\mathrm{b}|}$ and $T_{\mathrm{b}\odot}$ are, respectively, the linear and circular coherent components. $\hat{T}$ is source function in Kelvin and $\mathbf{G}$ is a propagation matrix given by

$$\mathbf{G} = \frac{\mathrm{i}2\pi v}{c}\sum_{\Delta M=-1}^{1}\rho_{\Delta M}(\theta,\phi)\sum_{M}\tilde{N}_{M,\Delta M}(v), \quad (3)$$

where $\tilde{N}_{M,\Delta M}(v)$ is the complex index of refraction due to a particular Zeeman component, c is the speed of light, and (θ,ϕ) describe the angles between the magnetic field and the direction of propagation. The three transitions, $\Delta M = -1, 0$, and 1, are also known as σ_-, π and σ_+ components with $\rho_{\Delta M}(\theta,\phi)$ matrix for each transition. On the linear polarization basis, $\rho_{\Delta M}(\theta,\phi)$ matrices are given by

$$\rho_{\pm 1} = \begin{bmatrix} \cos^2\phi + \sin^2\phi\cos^2\theta & -\sin\phi\cos\phi\sin^2\theta \mp \mathrm{i}\cos\theta \\ -\sin\phi\cos\phi\sin^2\theta \pm \mathrm{i}\cos\theta & \sin^2\phi + \cos^2\phi\cos^2\theta \end{bmatrix}, \quad (4)$$

$$\rho_0 = \begin{bmatrix} \sin^2\phi\sin^2\theta & \sin\phi\cos\phi\sin^2\theta \\ \sin\phi\cos\phi\sin^2\theta & \cos^2\phi\sin^2\theta \end{bmatrix}. \quad (5)$$

A special case ($\phi=0$) was given in Lenoir (1968) who made early attempt to establish the technique of sounding mesospheric temperature. The solution to Eq. (2) between initial point s_0 and ending point s can be written as

$$\mathbf{T}_{\mathrm{b}}(s) = \mathbf{T}_{\mathrm{b}}(s_0)\,\Upsilon(s_0) + \hat{T}(s_0)[\mathbf{I}-\boldsymbol{\Upsilon}(s_0)] + \int_{\hat{T}(s)}^{\hat{T}(s_0)}\boldsymbol{\Upsilon}(\hat{T})\,\mathrm{d}\hat{T}, \quad (6)$$

where $\mathbf{I}$ is the identity matrix, $\boldsymbol{\Upsilon}\equiv\boldsymbol{\tau}\boldsymbol{\tau}^{\dagger}$ is the transmission function matrix, and the product matrix is defined as

$$\boldsymbol{\tau} = \exp\left[-\int_{s_0}^{s}\mathbf{G}(s')\,\mathrm{d}s'\right]. \quad (7)$$

The evaluation of this matrix can be readily carried out with the expressions described in Rosenkranz and Staelin (1988), where $\rho_{\Delta M}(\theta,\phi)$ matrices are projected onto the right- and left-circular polarization basis.

3.2. Numerical calculations

In limb viewing cases it is convenient to divide the integration in Eq. (6) into two parts: one from space ($s=0$) to

tangent point, and the other from tangent point to MLS receiver. The discrete model atmosphere, labeled by $i = 1$ at the surface and $i = n$ at the top ($\sim$140 km), is assumed to have a set of evenly-spaced spherically-homogenous layers such that we can re-write Eq. (6) as

$$\mathbf{T}_{bn} = \sum_{i=n}^{t} \Delta\hat{T}_i \boldsymbol{\Upsilon}_{n-i+1} - \sum_{i=t}^{n} \Delta\hat{T}_i \boldsymbol{\Upsilon}_{n+i} + \hat{T}_{\text{space}} \boldsymbol{\Upsilon}_{2n}, \quad (8)$$

where t is the tangent layer. $\boldsymbol{\Upsilon}$ has been defined above and $\boldsymbol{\tau}$ at each layer is evaluated from the following recursive relations:

$$\tau_{n-i+1} = \tau_{n-i}\Delta\tau_i,$$

$$\tau_{n+i} = \tau_{n+i-1}\Delta\tau_{i-1},$$

$$\tau_1 = \Delta\tau_n = \mathbf{I}$$

and the increments of the source function are given by

$$\Delta\hat{T}_i = 0.5[\hat{T}_{i-1} - \hat{T}_{i+1}],$$

$$\Delta\hat{T}_1 = 0.5[\hat{T}_{\text{surface}} - \hat{T}_2],$$

$$\Delta\hat{T}_n = 0.5[\hat{T}_{n-1} + \hat{T}_n].$$

Since the propagation matrix is proportional to volume mixing ratio, the incremental transmission has the form

$$\Delta\tau_i = \exp\left[-\sum_l \sum_{\Delta M=-1}^{1} \int_{s_{i+1}}^{s_i} \rho_{\Delta M}(\theta,\phi)\beta^l_{i\Delta M} f^l \, \mathrm{d}s\right], \quad (9)$$

where f^l is the mixing ratio function and l is the index for species. $\beta^l_{i\Delta M}$ is the "cross section" or the absorption coefficient derivative with respect to mixing ratio, which depends on atmospheric temperature and geomagnetic field.

3.3. Line absorption model

The derivative of the absorption coefficient with respective to mixing ratio or the "cross-section", in km^{-1}, is given by

$$\beta_{i\Delta M} = 3.402136 \times 10^9 \frac{p_i}{T w_{\text{d}}^j} \left\{ \sum_j \left[\mathfrak{I}_j \frac{Q(300\text{ K})}{Q(T)} \times \frac{1 - \exp(hv_j/kT)}{1 - \exp(hv_j/300k)} 10^{\frac{E_j}{1.600386}\left(\frac{1}{300} - \frac{1}{T}\right)} \right] \times \text{Voigt}_{i\Delta M}(x_j, y_j, z_j) \right\}, \quad (10)$$

where T is air temperature in K, p_i is pressure in hPa, $\mathfrak{I}_j$ is the integrated intensity at 300 K in nm^{2}MHz, v_j is the line center frequency in MHz, E_j is the ground state energy of transition in cm^{-1}, $Q(T)$ is the temperature-dependent partition function in MHz, and $\omega_{\text{d}}^j \approx 3.5811737 \times 10^{-7} v_j \sqrt{T/m}$ is the Doppler line width for the molecule of mass number m. The Voigt function is used to model the lineshape at all altitudes and is given by

$$\text{Voigt}_{i\Delta M}(x_j, y_j, z_j) = \left(\frac{v}{v_j}\right)^2 \int_{-\infty}^{\infty} \frac{\mathrm{e}^{-t^2}}{\pi} \sum_{M=-N}^{N} \frac{\xi_{j,M,\Delta M}}{(x_{j,M,\Delta M} - t)^2 - y_j^2} \times \{y_j - Y_j(x_{j,M,\Delta M} - t) + i(y_j Y_j + x_{j,M,\Delta M} - t)\} \, \mathrm{d}t. \quad (11)$$

Table 2
Magnetically perturbed O_2 line frequencies (in MHz) and strength relative to zero field values

	$\Delta v_{j,M,\Delta M}$	$\xi_{j,M,\Delta M}$
$\sigma_\pm$	$-2.8026B\dfrac{M(N-1)\pm N}{N(N+1)}$	$\dfrac{3(N\pm M+1)(N\pm M+2)}{4(N+1)(2N+1)(2N+3)}$
π	$-2.8026B\dfrac{M(N-1)}{N(N+1)}$	$\dfrac{3[(N+1)^2+M^2]}{(N+1)(2N+1)(2N+3)}$

The magnitude of magnetic field B is in gauss.

The interference coefficients, which are assumed unvarying with magnetic field and among the Zeeman components, are parameterized in Liebe (1992) as

$$Y_j = p_i \left\{ \delta_j \left(\frac{300}{T}\right)^{0.8} + \gamma_j \left(\frac{300}{T}\right)^{1.8} \right\} \quad (12)$$

and

$$x_{j,M,\Delta M} = \sqrt{\ln 2}(v_j - v + \Delta v_{j,M,\Delta M})/\omega_{\text{d}}^j,$$

$$y_j = \sqrt{\ln 2}(300/T)^{n_j} \omega_{\text{c}}^j p_i/\omega_{\text{d}}^j, \quad (13)$$

where ω_{c}^j is the collision line width at 300 K and 1 hPa, n_j is its temperature dependence, $\Delta v_{j,M,\Delta M}$ and $\xi_{j,M,\Delta M}$ are the magnetically perturbed frequency offset and line intensity. The values of $\Delta v_{j,M,\Delta M}$ and $\xi_{j,M,\Delta M}$ are listed in Table 2 for the N^+ lines.

The convolution with the instrument filters in Eq. (1) is carried out with 25 points around the filter shape over a frequency range twice the measured 3 dB channel width in Table 1. The 25-point convolution is tested and gives error less than 1 K in the radiances at tangent heights below $\sim$90 km, which is apparently benefited from the strong overlapping among the Zeeman lines (Hartmann et al., 1996). The convolution with the instrument FOV is performed with the measured pattern that spans over $\sim 11^\circ$ and is re-sampled in 512 points.

3.4. Fast model

The MLS radiative transfer model is nonlinear about the geomagnetic field $\boldsymbol{B}$ and calculations for temperature

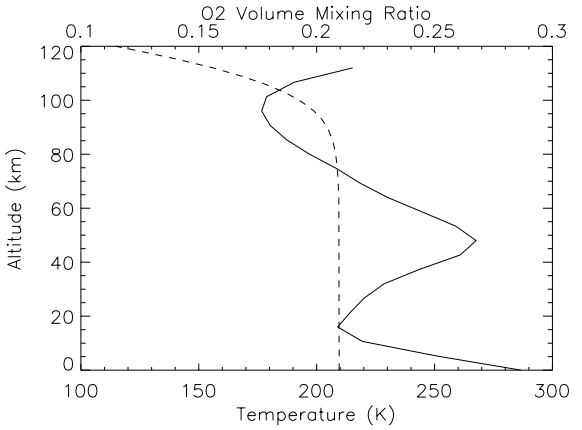

Fig. 2. Temperature (solid) and O_2 mixing ratio (dashed) profiles used as the linearization bases of MLS forward model and also as the a priori in the retrieval. The temperature profile is the annual mean of CIRA'86 (COSPAR International Reference Atmosphere), and the O_2 profile is the annual mean of MSISE90 (Mass Spectrometer Incoherent Scatter Radar Extended) model (Hedin, 1991).

derivatives (i.e., weighting functions) can be time consuming. In order to make the temperature retrieval algorithm practical for processing several years of the data, the forward model needs to be fast enough for each call on a geomagnetic field case. One solution for the fast model is to approximate the model with the first-order Taylor expansion. If the radiance model has the form $T^{\mathrm{A}}_{\mathrm{b}\|}=F(p,T,f^l,\boldsymbol{B})$, we first linearize it on tangent pressure p, temperature T and mixing ratio f^l as the first order Taylor expansion

$$T^{\mathrm{A}}_{\mathrm{b}\|} \approx F(p_0,\mathbf{T}_0,\boldsymbol{f}^l_0,\boldsymbol{B}) + F'_p(p_0,\mathbf{T}_0,\boldsymbol{f}^l_0,\boldsymbol{B})(p-p_0) + F'_T(p_0,\mathbf{T}_0,\boldsymbol{f}^l_0,\boldsymbol{B})(\mathbf{T}-\mathbf{T}_0) + \sum_l F'_{f^l}(p_0,\mathbf{T}_0,\boldsymbol{f}^l_0,\boldsymbol{B})(\boldsymbol{f}^l-\boldsymbol{f}^l_0), \quad (14)$$

where p_0 is the pre-selected tangent pressure, $\mathbf{T}_0$ and $\boldsymbol{f}^l_0$ are the linearization profiles on p_0 (Fig. 2). The partial derivatives, $F'_p(p_0,\mathbf{T}_0,\boldsymbol{f}^l_0,\boldsymbol{B})$, $F'_T(p_0,\mathbf{T}_0,\boldsymbol{f}^l_0,\boldsymbol{B})$ and $F'_{f^l}(p_0,\mathbf{T}_0,\boldsymbol{f}^l_0,\boldsymbol{B})$, are also known as weighting functions for p, $\mathbf{T}$ and $\boldsymbol{f}^l$, respectively. For the temperature retrieval, only O_2 mixing ratios are important in Eq. (14) and allowed to vary at heights above ~80 km. Now, we need a fast algorithm to obtain the Taylor expansion coefficients in Eq. (14) for each case of the geomagnetic field $\boldsymbol{B}$. This is developed as follows.

First, the Taylor coefficients $F'_T(p_0,\mathbf{T}_0,\boldsymbol{f}^{\mathrm{O_2}}_0,\boldsymbol{B})$ are calculated with the finite difference method where we perturb $\mathbf{T}$ values one at a time for 22 pressure levels [$z_T = -\log(p_T) = -3 + i/3,\ i = 0,1,\ldots,21$] between the surface and ~120 km and repeat the calculation for 43 tangent pressures [$z=-\log(p_0)=-3+i/6,\ i=0,1,\ldots,42$]. Coefficients $F'_{f_{\mathrm{O_2}}}(p_0,\mathbf{T}_0,\boldsymbol{f}^{\mathrm{O_2}}_0,\boldsymbol{B})$ are calculated at 21 pressure levels [$z_{\mathrm{O_2}}=-\log(p_{\mathrm{O_2}})=(-3,1+0.2i,\ i=0,1,\ldots,19)$], where p_T, p_0, and $p_{\mathrm{O_2}}$ are in hPa. Coefficients $F(p_0,\mathbf{T}_0,\boldsymbol{f}^{\mathrm{O_2}}_0,\boldsymbol{B})$ are the radiances at the linearization points, and $F'_p(p_0,\mathbf{T}_0,\boldsymbol{f}^{\mathrm{O_2}}_0,\boldsymbol{B})$ are the derivatives of radiance with respect to tangent pressure. These calculations are carried out only for single temperature and O_2 profiles but in 220 geomagnetic cases: 4B-bins (0.25, 0.35, 0.45, 0.55 G), 5 θ-bins (between 0 and π) and 11ϕ-bins (between 0 and 2π).

Second, we computed the Taylor coefficients of the 220 cases to a set of basis functions expressed in the following:

$$\{1,(B-B_0),(B-B_0)^2,(B-B_0)^4,g(B-B_0)\} \otimes \{1,\cos 2\phi,\sin 2\phi\} \otimes \{1,\cos 2\theta,\sin 2\theta,\sin\theta\}, \quad (15)$$

where

$$B_0 = 0.4\ \mathrm{G},$$

$$g(x) = \begin{cases} x^3 & \text{ch. 6, 7, 10,} \\ \cos(2\pi x/0.5 - 0.1) & \text{ch. 8,} \\ \cos(2\pi x/0.2 - 1.2) & \text{ch. 9.} \end{cases}$$

These basis functions are chosen to best fit the geomagnetic-field dependence of the Taylor coefficients over the entire altitude range (0–140 km), and the fitting coefficients are stored as part of the fast forward model, which will be used later in the temperature retrieval. No geomagnetic calculations for ch. 1–5 and ch. 11–15 since there is little effect from the geomagnetic field. Note that the basis functions associated with angle ϕ have relatively simple forms because of the rotation symmetry in the polarization matrix. We found good accuracy (~1 K) with the fast model when reproducing the full radiative transfer calculations.

3.5. Hydrostatic balance constraint

Along with the radiance measurements, MLS also measures tangent height using the antenna position reading and information from the spacecraft attitude determination system. The tangent height measurement can be used to constrain the temperature and tangent pressure retrievals through the hydrostatic balance assumption, namely,

$$\mathrm{d}h = \frac{R\ln 10}{g}\,T\,\mathrm{d}z, \quad (16)$$

where h is tangent height, g is the gravitational acceleration, R is the gas constant for dry air (=287 J K^{-1} kg^{-1}), and $z=-\log(p)$ for tangent pressure in hPa.

4. Inversion method and analysis

4.1. Optimal solution

The linearized radiative transfer model Eq. (15) and the hydrostatic balance constraint Eq. (16) can be combined in

Table 3
O_2 line parameters used in MLS forward model

N^+	v (MHz)	log Q			ω_c^j (MHz/hPa)	n_j	E_j (cm^{-1})	log $\Im^l$ (300 K)
		300 K	225 K	150 K				
15+	62 997.971	2.3398	2.2152	2.0398	1.211	0.8	343.7484	−6.6076
17+	63 568.520	2.3398	2.2152	2.0398	1.182	0.8	438.4418	−6.7441

a generalized form

$$\mathbf{y} = \mathbf{y}_0 + \mathbf{K}(\mathbf{x} - \mathbf{x}_0) + \boldsymbol{\varepsilon}_y, \tag{17}$$

where $\mathbf{y}$ is known as the measurement vector containing limb radiances and tangent heights, and $\boldsymbol{\varepsilon}_y$ is the uncertainty associated with these measurement. In this study, the radiance uncertainties in $\boldsymbol{\varepsilon}_y$ are inflated slightly (adding 1.4 K to the measurement precision for each channel) to reflect forward model error and other unknown errors. For the tangent height measurements, we only use the height differences between adjacent pointings since the absolute pointing accuracy (1–2 km) is much worse than its precision (~30 m). In the measurement error vector $\boldsymbol{\varepsilon}_y$, hence, the uncertainty is set as ~50 m for the height differences. Beside the measurement vector in Eq. (17), $\mathbf{x}$ is known as the state vector composed of all the quantities to be retrieved: tangent pressure, temperature, O_2 mixing ratio, and a baseline radiance that accounts for excessive radiation from the antenna spillover. In addition, $\mathbf{y}_0$ is the forward model solution at $\mathbf{x} = \mathbf{x}_0$ and $\mathbf{K}$ is the derivatives (or weighting functions) of $\mathbf{y}$ with respect to $\mathbf{x}$.

The inversion of $\mathbf{x}$ is based on the standard optimal estimation approach shown in (Rodgers, 1976)

$$\hat{\mathbf{x}} = \mathbf{x}_0 + [\mathbf{S}_a^{-1} + \mathbf{K}^T\mathbf{S}_y^{-1}\mathbf{K}]^{-1} \times [\mathbf{S}_a^{-1}(\mathbf{a} - \mathbf{x}_0) + \mathbf{K}^T\mathbf{S}_y^{-1}(\mathbf{y} - \mathbf{y}_0)], \tag{18}$$

where $\hat{\mathbf{x}}$ is an optimal solution to $\mathbf{x}$ in Eq. (17), $\mathbf{a}$ is the a priori estimate of $\mathbf{x}$, $\mathbf{S}_a$ and $\mathbf{S}_y$ are covariance matrices for $\mathbf{a}$ and $\mathbf{y}$, respectively. For convenience we set $\mathbf{a} = \mathbf{x}_0$ in this study. The uncertainty of a priori temperature is 10 K everywhere except 6 K at 100 hPa and 1 K at pressures above 100 hPa. The uncertainty for a priori tangent pressure is 300 m for the initial pointing profile.

The temperature and tangent pressure retrievals are proceeded in an iterative way as follows. It first starts with the a priori temperature and O_2 profiles, as shown in Fig. 2, to establish the a priori tangent pressure using the tangent height measurements and the hydrostatic balance assumption. Then, the fast model is called for the geomagnetic field at this location, and the model radiances and weighting functions are interpolated onto the estimated tangent pressures. The International Geomagnetic Reference Field (IGRF) model (Barraclough, 1986) is used to obtain the field parameters. Now, the system is ready for the retrieval. In the first retrievals for temperature and tangent pressure, tangent pressures receive significant updates since they are the most sensitive variables. However, the top and bottom of tangent pressures remain inaccurate after the first retrieval and need iterative steps to improve. In the second iteration of the retrieval, we interpolate the same model radiances and weighting functions onto the newly retrieved tangent pressures, and repeat the temperature and tangent pressure inversions as in the first retrieval. By iterating these procedures several times, we quickly improve the temperature and tangent pressure retrievals. Convergence is generally found within 3–5 iterations, and the final tangent pressure, temperature and O_2 mixing ratio profiles are output as the retrieval solution.

4.2. Estimated precision and vertical resolution

A useful measure of retrieval performance and sensitivity is the matrix called averaging kernel, which can be computed with the following equation:

$$\frac{\partial \hat{\mathbf{x}}}{\partial \mathbf{x}_0} = [\mathbf{S}_a^{-1} + \mathbf{K}^T\mathbf{S}_y^{-1}\mathbf{K}]^{-1}\mathbf{K}^T\mathbf{S}_y^{-1}\mathbf{K}. \tag{19}$$

The rows of this matrix are the response of the retrieval system to a delta-function perturbation in the state vector. The columns of the matrix describe relative importance of different parts of the atmosphere to each retrieval level. The width of such response in each column provides an estimate of the vertical resolution of retrieved quantities (Table 3).

The averaging kernel may vary somewhat from profile to profile but general properties remain similar. In Fig. 3 is a typical averaging kernel for temperature retrieval showing the sensitivity degradation above ~60 km where only channels 7–9 are contributing. The sensitivity decreases further above ~85 km as channel 8 becomes the only contributing measurement. Table 4 gives the estimated precision of MLS temperature, $\sigma_{\hat{x}}^2 = \mathrm{Diag}\{[\mathbf{K}^T\mathbf{S}_y^{-1}\mathbf{K}]^{-1}\}$, which excludes the a priori part and only accounts for the MLS contribution. The sharp degradation in precision above ~90 km indicates severe loss of MLS temperature sensitivity, which would drive temperature retrievals very close to the a priori value. The temperature retrieval is best between 20 and 60 km showing precision of ~4 to ~7 K but the uncertainty increases

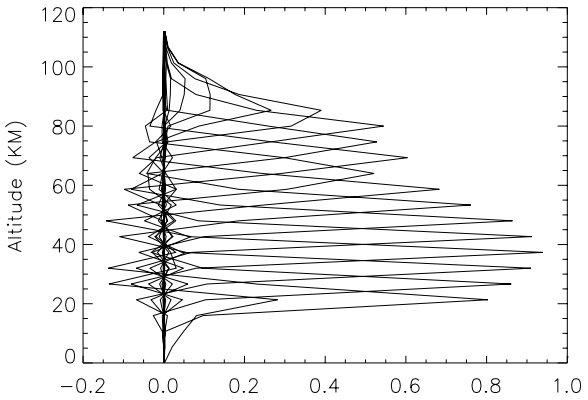

Fig. 3. An example of averaging kernel in MLS temperature retrieval, taken from the columns of the averaging kernel matrix. In this case the tangent heights of MLS scan ranges between 90 km and the surface, and all the radiance measurements are used.

Table 4
Estimated precision and vertical resolution of MLS temperature

Level	Approx. height (km)	Precision (K)		Vertical res. (km)	
		$B = 0.25$ G	$B = 0.63$ G	$B = 0.25$ G	$B = 0.63$ G
19	101.3	66	48	13.0	16.5
18	96.0	27	23	13.0	17.0
17	90.7	13	15	13.0	13.0
16	85.3	8.7	8.6	14.0	12.5
15	80.0	8.2	6.1	14.5	10.5
14	74.7	7.7	6.0	15.5	11.5
13	69.3	7.1	4.9	14.0	10.5
12	64.0	6.6	5.9	12.5	12.0
11	58.7	3.9	4.0	9.5	9.5
10	53.3	2.9	3.4	8.0	8.5
9	48.0	2.0	2.3	7.0	7.5
8	42.7	1.8	1.8	7.0	7.5
7	37.3	1.5	1.5	7.5	7.5
6	32.0	1.3	1.3	7.0	7.0
5	26.7	1.4	1.3	7.5	7.5
4	21.3	2.3	2.3	8.0	7.5
3	16.0	5.8	5.7	6.5	6.5

to ~9 K near 85 km and ~13 K near 90 km. Accordingly, the vertical resolution also degrades in the similar trend at these heights. The temperature precision differs slightly between strong and weak geomagnetic field cases. Most of the differences are seen in the mesosphere due to field-sensitive weighting functions of channels 7–9. It should be noted in Fig. 3 that MLS channels in the 63 GHz radiometer are not optimal for sounding the mesospheric temperature. Narrower filters and more frequency channels around the line center would have provided a better temperature sounding in the mesosphere.

At the low altitude end, MLS temperature sensitivity diminishes at ~100 hPa or ~16 km due to the limited bandwidth (~500 MHz) of the 15-channel filterbank. The radiances from the wing channels are saturated at ~20 km tangent height as a result of the pressure broadening. The loss of the sensitivity is reflected in the averaging kernel showing sharp rise in the estimated temperature error. Unlike the early versions of MLS retrievals, this algorithm does not constrain temperature to NCEP (the National Center for Climate Prediction) values at altitudes below ~20 km. Instead, the temperature is constrained to the a priori values given in Fig. 2, which is constant everywhere for all the data processed. A slightly loose constraint (6 K) is used at 16 km to ensure the stable retrieval at ~20 km. Below ~16 km the constraint is tightened (1 K) to the a priori to prevent the retrieval from becoming unstable.

Table 5
Estimated precision of MLS tangent pressure

Log pressure $z = -\log(p/\text{hPa})$	Approx. ht. (km)	Est. precision (km)	
		$B = 0.25$ G	$B = 0.63$ G
2.8494	93.6	0.644	0.347
2.2345	83.8	0.479	0.309
1.7276	75.6	0.297	0.282
1.2311	67.7	0.120	0.187
0.8301	61.3	0.075	0.104
0.4948	55.9	0.060	0.068
0.1846	51.0	0.055	0.056
−0.0217	47.7	0.049	0.052
−0.2347	44.2	0.043	0.044
−0.4502	40.8	0.038	0.039
−0.6217	38.1	0.034	0.034
−0.7965	35.3	0.033	0.032
−0.9715	32.5	0.039	0.037
−1.1538	29.5	0.056	0.052
−1.3367	26.6	0.097	0.093
−1.4945	24.1	0.184	0.179
−1.5999	22.4	0.302	0.275
−1.6736	21.2	0.474	0.499
−1.7677	19.7	0.962	0.845
−1.8437	18.5	1.736	1.900
−1.9322	17.1	1.959	3.139
−1.9138	17.4	2.281	0.550
−2.1894	13.0	0.396	0.428
−2.4441	8.9	0.355	0.368
−2.6615	5.4	0.323	0.335
−2.8865	1.8	0.290	0.288

Table 5 gives the estimated precision for the retrieved tangent pressures where the best pointing sensitivity is around $z = -0.8$ or $p = 6.3$ hPa showing a precision of 33 m. The error increases at higher and lower altitudes as the line width becomes either too narrow or too wide relative to the bandwidth of MLS channels. A large uncertainty (1–3 km) near 100 hPa is apparently caused by the tightened temperature a priori uncertainty, which is coupled to pressure through the hydrostatic balance constraint.

4.3. Result and analysis

Fig. 4 displays the MLS temperature retrieval in the mesosphere on January 8, 1992, showing a strong wave 2 pattern in the Northern Hemisphere. The pattern is found consistent to the independent observations of UARS ISAMS (Improved Stratosphere and Mesosphere Sounder) on the same day. The wave rotates clockwise with a warm core centered near the North Pole while the amplitude decreases with altitude. At 0.022 hPa (∼75 km), the wave 2 structure disappeared, left with some patchy features and a warm center. The center temperature seems somewhat warmer in the MLS observation than in ISAMS as found later due to a warm MLS bias.

In Fig. 5 we summarize the MLS data and coverage with the time series of daily mean temperatures at selected latitudes and altitudes. MLS had a nearly continuous operation before 1995 and then experienced some observing gaps due to spacecraft and instrument malfunctions in the following years. At high latitudes (top and bottom panels) the annual variation dominates with several warming events at 50 km during January in the Northern Hemisphere and July in Southern Hemisphere. Large data gaps are also evident as a result of UARS periodic yaw maneuvers. As shown in the middle panel of Fig. 5, the semiannual and quasi-biannual variations are clearly dominating the equatorial temperature variations at 50 and 20 km, respectively. These variations are not so predominant at 85 km where a cooling trend (∼1 K/year) appears during 1991–1997, which is likely impacted by the first half of the solar cycle. This cooling trend has also showed up in the saturated Ch.8 radiances that cover uppermost altitudes in the MLS height coverage. The saturated MLS radiances, which have little sensitivity to tangent pressure, are good measure of air temperature of the saturation layer. For channel 8, the saturation layer is ∼15 km thick centered around 80 km.

A useful quality indicator for the retrieval system is the χ^2 of the radiance residuals after retrieval fitting. As shown in Fig. 6, the daily averaged χ^2 reflects the goodness of fit between the modeled and the measured radiances. At low latitudes the χ^2 varies slightly around 0.7, showing not only the semiannual variation but also the distinct cycle synchronous to the UARS yaw period. The χ^2 is slightly higher near the yaw days when the instrument temperature rises due to more illumination from the Sun. In other words, the forward model fits the radiance measurements relatively poorly near those days around the yaw maneuvers. The yaw cycle variation in the χ^2 may indicate potential degradation in the retrieved temperature and tangent pressure. However, such degradation is difficult to quantify since the yaw-cycle variation is coupled to the diurnal and semidiurnal tides in MLS sampling. The yaw cycle χ^2 variation also appears at high latitudes but with a less degree of significance due to large seasonal variations. At high latitudes the χ^2 exhibits a strong seasonal variation with large values in the winter months. The increasing χ^2 is primarily a result of small-scale wave activity that enhances the radiance fluctuations within a single scan (Wu and Waters, 1996). Since the temperature retrieval assumes homogeneous atmospheric layers within each scan, these small-scale fluctuations act as additional noise to the measurement system and cause the χ^2 increase. The χ^2 can also increase if the real temperature departs too far from the linearization profile used. It is interesting to note that the χ^2 is greater in the southern winter than in the northern winter, which may result from a combination of enhanced wave activity and a greater number of extreme temperature profiles.

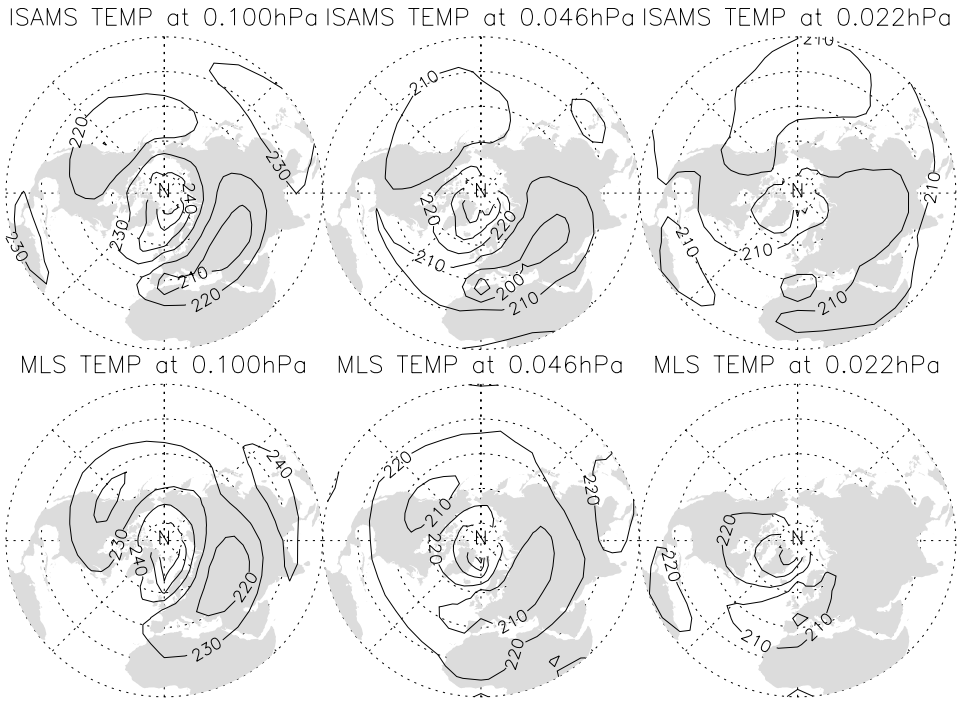

Fig. 4. A major planetary wave perturbation observed by MLS and ISAMS on January 8, 1992 in the Northern Hemisphere, showing consistent patterns between the two measurements in the mesosphere. Temperatures are contoured at 10 K intervals and latitude cycles are indicated every 20° from the equation.

5. Comparisons to other measurements

In this section we provide a validation of the new MLS temperature retrieval against observations from CIRA'86 (COSPAR International Reference Atmosphere) climatology, ISAMS, HRDI (High Resolution Doppler Imager), CRISTA1 (Cryogenic Infrared Spectrometers and Telescopes for the Atmosphere-1), lidars and rockets. In these comparisons, we try to establish as many "coincident" observations as possible between MLS and the correlative measurements to evaluate potential biases in the MLS temperature.

5.1. MLS-CIRA

The CIRA'86 monthly climatology (Fleming et al., 1990) is used to compare to the MLS temperature climatology obtained between 1991 and 1994. Fig. 7 shows the MLS-CIRA comparisons for temperatures and differences averaged on a seasonal basis (nominally for December–February, March–May, June–August, September–November). Since MLS retrieval is based on the linearization on a single temperature profile and independent of the CIRA climatology, it is very encouraging to obtain such similarity between the two datasets. Catching the seasonal temperature variability reflects good MLS sensitivity in the mesosphere and validity of the linear retrieval algorithm. Even under some extreme conditions like ones at summertime high latitudes, the linear retrieval is able to pull temperature as much as 40 K away from the initial guess at ~85 km. Moreover, the latitudinal temperature gradients are greater near 60°S in MLS temperature during JJA, reflecting strong influence of the polar vortex throughout the stratosphere and mesosphere. The differences in the latitudinal gradient in the mesosphere account for most of the biases at wintertime high latitudes. Near 90 km MLS has difficulty to fully recover very cold (e.g., 80°S during DJF) or very warm (e.g., 80°S during JJA) temperatures when the real profiles deviate far from the linearization values in Fig. 2. The retrieved temperatures tend to be biased closer to the linearization temperatures than the CIRA data in these cases, indicating a limitation of the linearized retrieval. This shortcoming can be overcome with multiple forward models linearized on different temperature profiles (for example, the CIRA climatology) such that the retrieval will use the linearization profile not too far from the truth. It would be ideal, if computing power allows, to run the full forward model interactively in each retrieval step to correct this nonlinearity problem.

A general cold bias appears in MLS temperatures at 80–90 km for all the seasons when compared to CIRA'86,

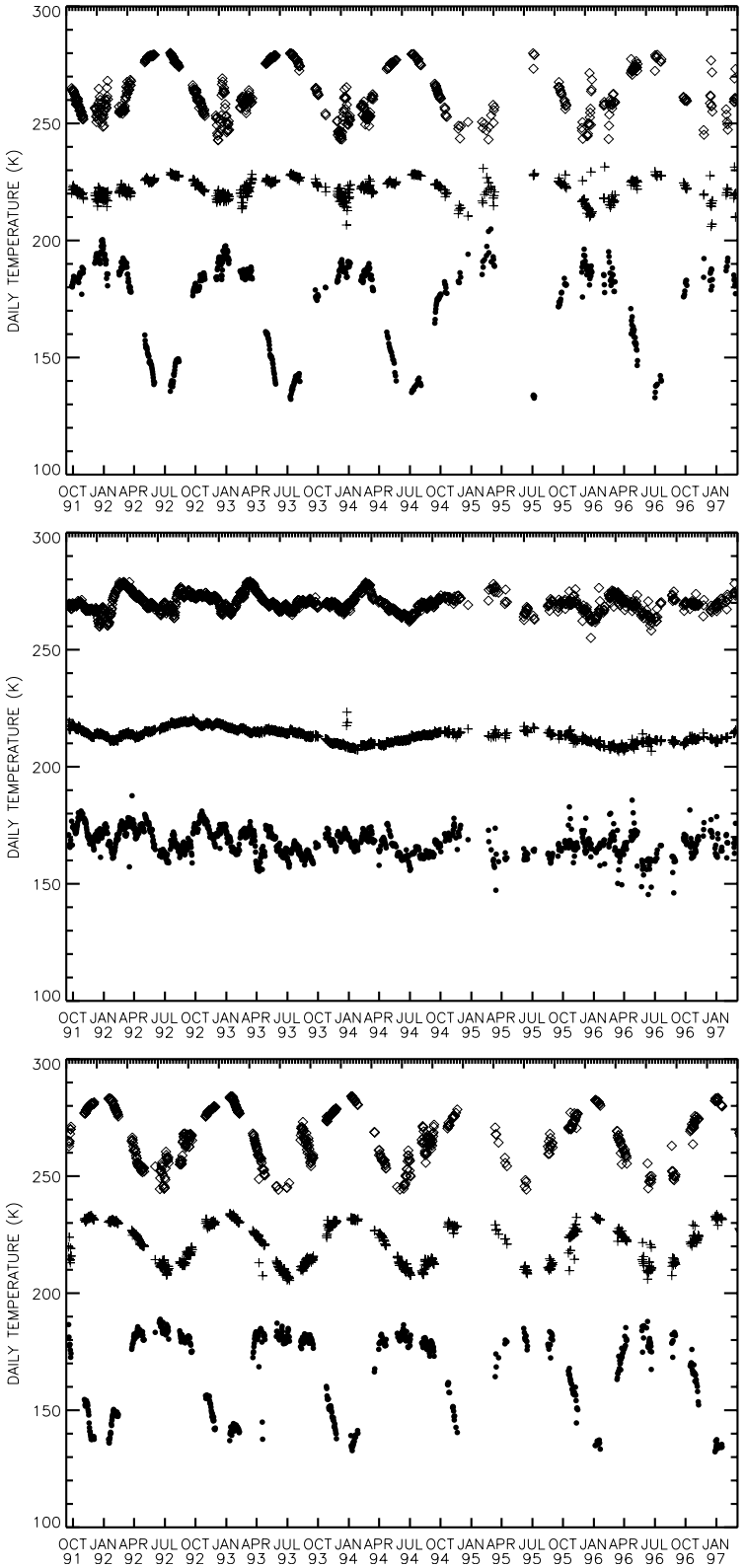

Fig. 5. Time series of MLS daily mean temperatures at approximate altitudes of 20 km (plus), 50 km (diamond), and 85 km (dot) during 1991–1997. The temperatures at 85 km are shifted down by 20 K to help illustration. The latitude bins are 5° apart and three latitudes are shown: 60°N (upper), equator (middle), and 60°S (lower). Large data gaps at the high latitudes are due to the UARS yaw maneuvers that produce biased MLS sampling in latitude.

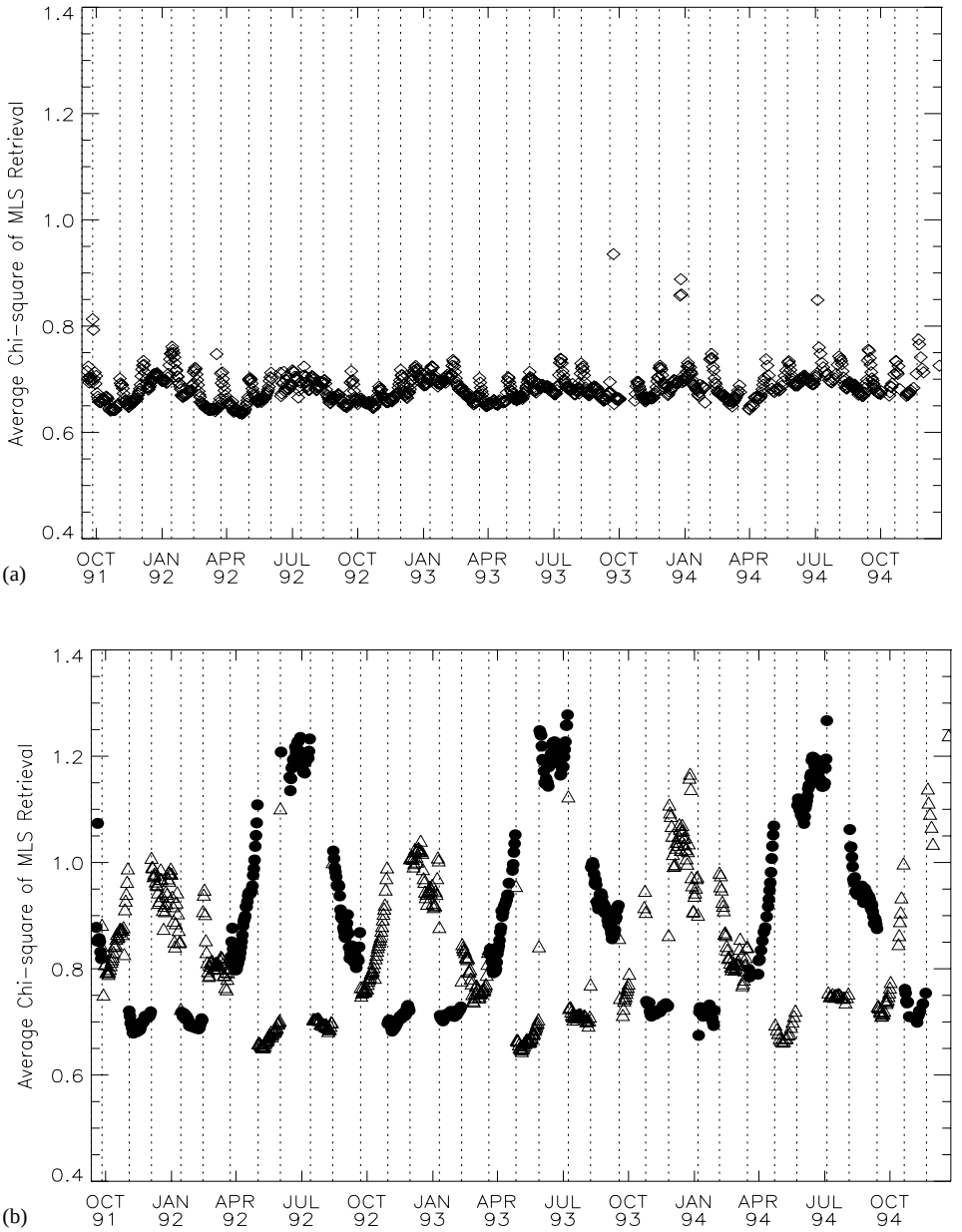

Fig. 6. Daily average χ^2 of the MLS radiance residuals at (a) low and (b) high latitudes. Triangles and filled circles in (b) represent the Northern and Southern Hemispheres, respectively. The χ^2 is normalized with inflated radiance error discussed in Section 4. The latitude of 35° is used to separate the latitude regions. The yaw days are highlighted with vertical dashed lines.

varying from −4 K at lower altitudes to −16 K at the top. A warm (∼4 K) and cold (∼4 K) bias are often seen near 60 and 40 km, respectively. Discontinuities at ±34° latitudes in the temperature differences, for example in JJA, are likely caused by incomplete sampling from UARS yaw maneuvers when MLS missed about 1 month of observations at high latitudes in each season.

5.2. MLS-ISAMS

The version 12 of ISAMS temperatures (essentially same as version 10) are used to compare with the MLS temperature. Also on board UARS, ISAMS measures temperature from the 15 μm CO_2 emission at 16–80 km altitudes with precision estimated between 2 and 12 K (Dudhia and Livesey, 1996; Livesey, 1995). The vertical resolution

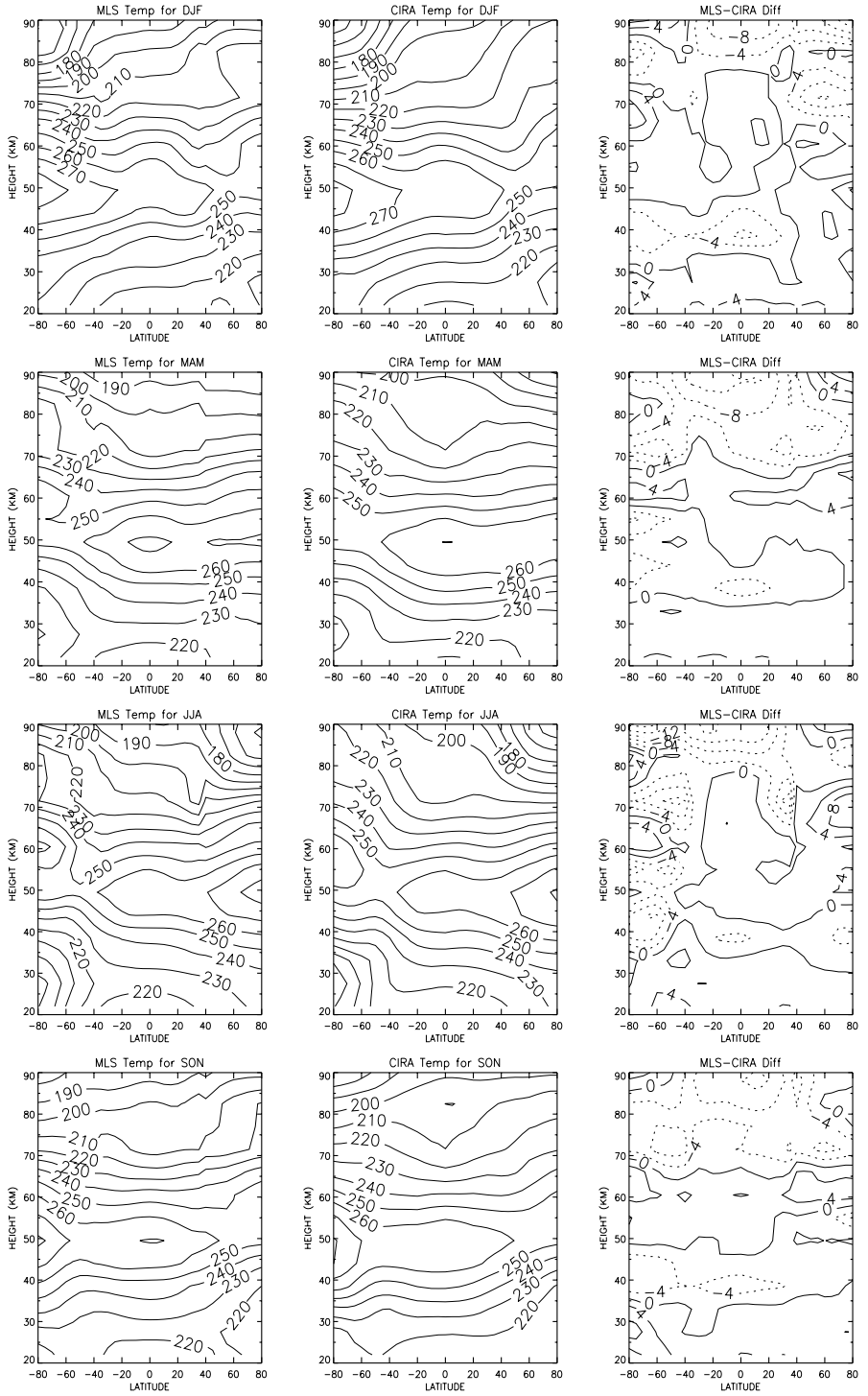

Fig. 7. Comparisons of MLS and CIRA'86 seasonal temperatures and differences as a function of latitude and height. The zonal mean temperatures are computed at MLS retrieval levels for 5° latitude bins and contoured at 10 K intervals. The difference contours are labeled every 4 K.

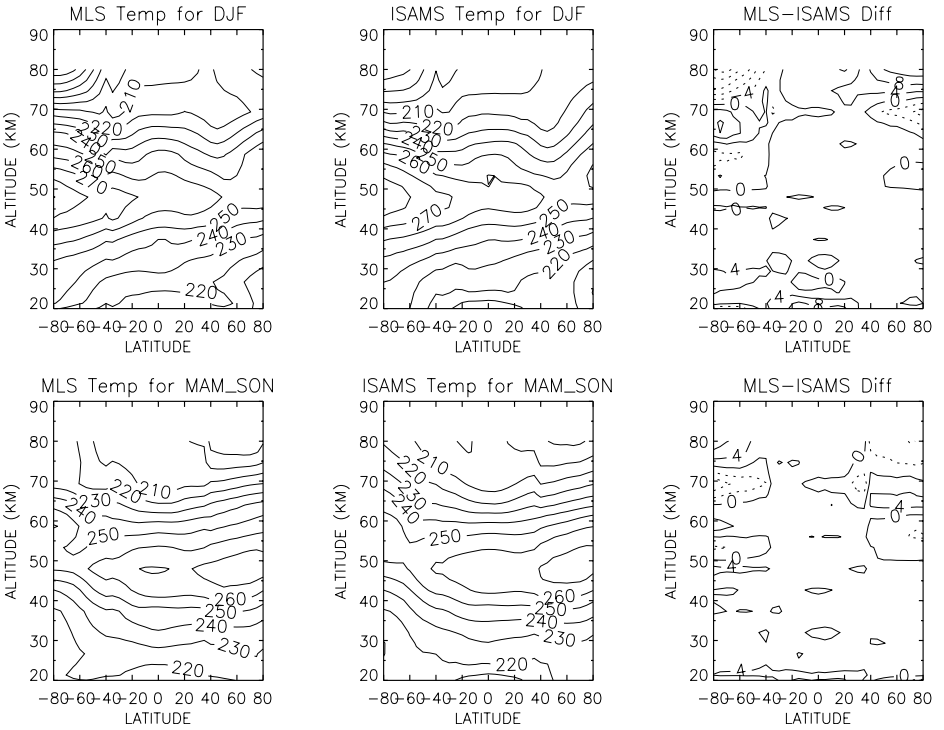

Fig. 8. Comparison of MLS and ISAMS "coincident" temperature measurements and differences in two seasons. The zonal means of the "coincident" temperatures are strongly biased in terms of sampling to the cases when the selection criteria are met. Contours of the zonal means are labeled every 10 K while the differences are plotted at 4 K intervals.

degrades with height from ~7 km in the stratosphere to ~20 km in the middle mesosphere (Fig. 8).

MLS-ISAMS comparisons are carried out for two seasons (DJF and MAM/SON) for all the data available during September 1991–May 1992 (ISAMS failed after May 1992). ISAMS viewing geometry is similar to MLS except that it can view both sides of the spacecraft. When both instruments were viewing the same side, their sampling volumes are very close in time and space. As a result, we have a large number of incidences even for the tight criteria for universal time ($|\Delta UT| < 10$ min), latitude ($|\Delta lat| < 2^\circ$), and longitude ($|\Delta lng| < 4^\circ$), applied to the "coincident" measurements.

MLS temperature in DJF shows a steeper vertical gradient between 60 and 80 km in the summer than ISAMS, which is similar to the MLS-CIRA comparison in this region. In the winter mesosphere MLS shows reversed temperature lapse rates between 60 and 90 km where they did not appear clearly in ISAMS, which cause the major differences in this region. The discontinuities at $\pm 34^\circ$ are also evident, which are likely caused by systematic errors between the two measurements. In the stratosphere, MLS is generally warmer than ISAMS by 1–2 K.

The mean MLS-ISAMS temperature differences oscillate somewhat in the upper mesosphere, showing a narrow band of low values across ~70 km at middle and low latitudes, which is not so prominent in the comparisons between MLS and CIRA'86. This difference, also shown in MLS-lidar comparisons, has been identified as a systematic error from MLS retrieval, which neglects the effect of Doppler shift due to the Earth rotation. The systematic effect is likely spread over to nearby altitudes, causing the warm bias of 2–4 K in MLS temperature near ~75 km. We will correct this error in the next version of the retrieval software.

5.3. MLS-HRDI

UARS HRDI measures the O_2 (0–0) band rotational temperature using the line strength ratios of two visible O_2 lines at altitudes of 65–105 km. The best temperature sensitivity (estimated 7 K error) is thought at altitudes above ~80 km. Below 80 km it has large (50%) influences from the a priori profiles used (Ortland et al., 1998). HRDI views 45° or 135° from the satellite velocity and therefore its measurements do not collocate with MLS or ISAMS at a given time. However, with somewhat looser criteria for the "coincident" measurements, i.e., $|\Delta UT| < 1$ h, $|\Delta lat| < 5^\circ$, and $|\Delta lng| < 10^\circ$, we may have a sufficient number of samples to compare. In addition, HRDI is a daytime instrument and

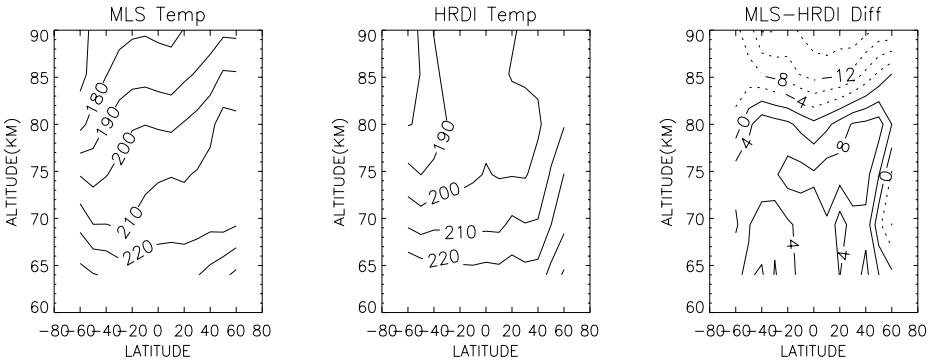

Fig. 9. Same as in Fig. 8 but for MLS-HRDI comparison.

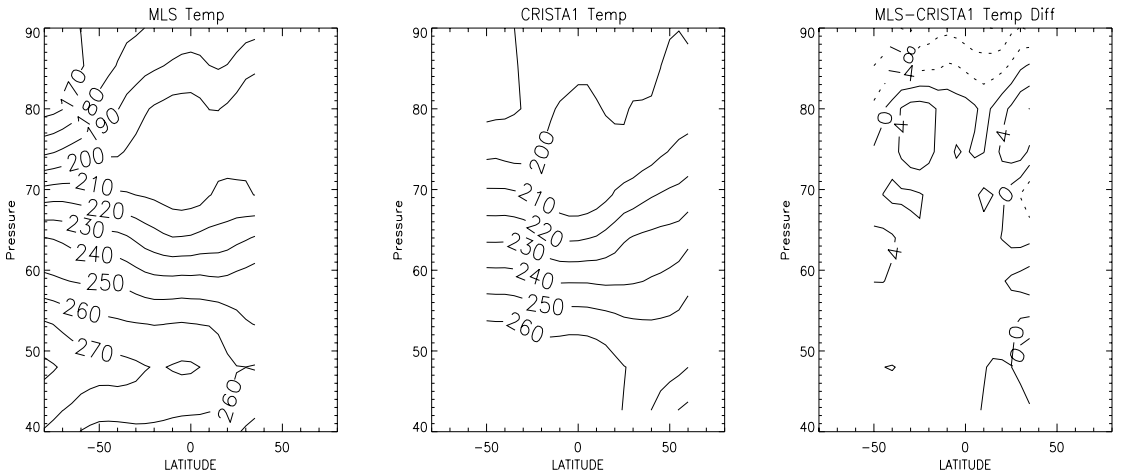

Fig. 10. Same as in Fig. 8 but for MLS-CRISTA1.

it is recommended to use data only with solar zenith angle greater than 70°.

MLS-HRDI comparisons are made for about 100 days of observations during October–December 1993. Above ~70 km, MLS temperature shows a steeper vertical gradient than HRDI at most latitudes, which reverses MLS biases from ~8 K warmer at ~70 km to ~16 K colder at ~90 km. Generally speaking, at altitudes where HRDI establishes good temperature sensitivity, MLS is colder almost everywhere with the coldest in the equatorial region at ~90 km. At latitudes greater than 50°N, HRDI temperature is likely affected more by high solar zenith angles, yielding the suddenly reversed differences at heights below 80 km (Fig. 9).

5.4. MLS-CRISTA1

Flown in early November 1994, the space-shuttle-based CRISTA1 obtains temperature from emissions near 12.6 μm at 20–55 km altitudes and 15 μm at 40–90 km altitudes with accuracy of ~1 and 1–2 K, respectively (Riese et al., 1999; G.A. Lehmacher, personal communication). In this comparison we only use the 15 μm measurements made during November 5–11, 1994.

We compared the 7-day (November 5–11, 1994) zonal means between the two datasets because the "coincidence" criteria like ones defined above are difficult to meet due to systematic shifts in the samplings by the two instruments. Since both instruments sampled both day and night with about 16 orbits per day, the effects of diurnal tide and slowly-moving planetary waves are expected to be reduced substantially in a zonal average (Oberheide et al., 2000), and hopefully the zonal mean differences can reflect the biases between the two datasets.

Similar to the MLS-ISAMS comparison, MLS shows a slightly warmer (4 K) bias near ~75 km but becomes colder (4–12 K) at ~90 km. However, these biases are subject to uncertainties caused by the sampling differences, including potential influence from the tidal waves. In particular, the semidiurnal tide can become significant in amplitude above 70 km to complicate the interpretation of the differences in Fig. 10. Oberheide et al. (2000) showed that the remaining

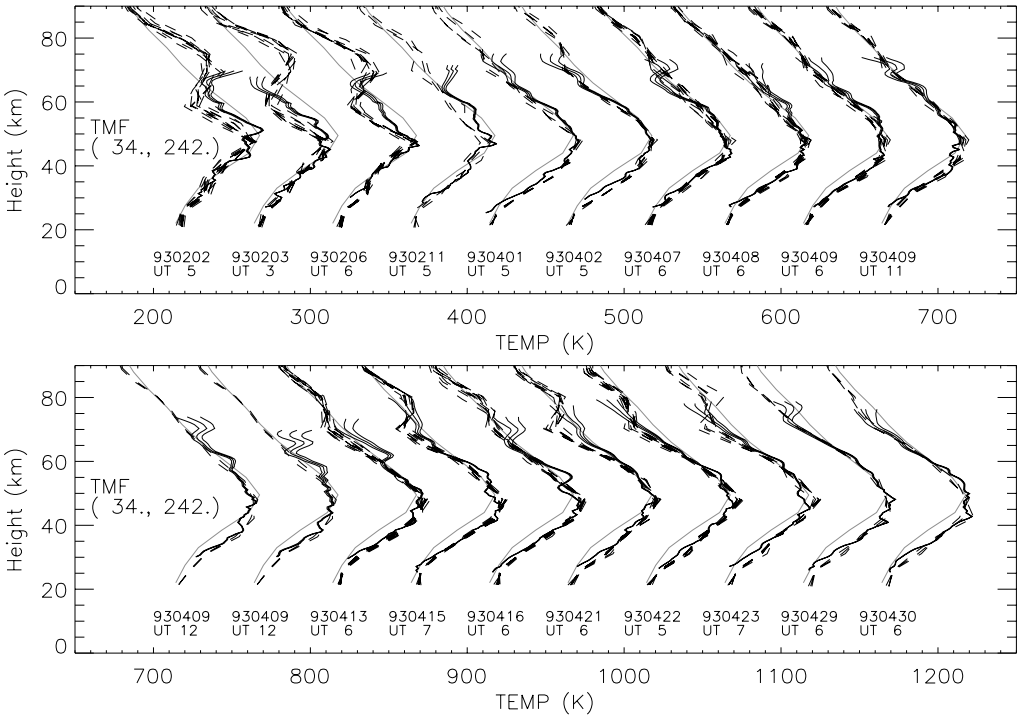

Fig. 11. Comparison of MLS and lidar temperatures at Table Mountain (34°N, 118°W). Selected individual profiles of "coincident" measurements are shown where MLS are in dashed line and lidar with uncertainty are in solid line. The thick line is the initial guess and also the linearization temperature profile used in MLS retrieval. The profiles are shifted by 50 K for each comparison.

effect of the semidiurnal tides in the CRISTA zonal mean can be as high as 1 K below 80 and 2 K at 80–90 km. Thus, the latitudinal variation of the MLS-CRISTA1 bias between 70 and 80 km is likely modulated by the remaining tidal effects under different samplings.

5.5. *MLS-lidars*

Several ground sites are used for MLS-lidar comparisons: Table Mountain, CA (TMF), Mauna Loa, Hawaii (MLO), Centre d'Essais des Landes, France (CEL), Observatoire de Haute Provence, France (OHP), Eureka (EUR), London, Canada (LON), and Colorado State University, Fort Collins, CO (CSU), which are all located in the Northern Hemisphere. Comparisons between MLS and lidar temperatures are all presented in the same format except for the CSU sodium lidar. The top 8 km of all Rayleigh-lidar temperature profiles are removed because they are often constrained tightly to the initial value/climatology used in the retrieval. The criteria of the "coincident" measurements are defined as $|\Delta UT| < 4$ h, $|\Delta lat| < 5^\circ$ and $|\Delta lng| < 10^\circ$ for all the sites. The looser temporal criterion helps to create more "coincident" cases since the lidar data are mostly nightly averages and some nights may have more measurements than others. By averaging the biases found in these "coincident" measurements, we hope to wash out short-scale and some tidal variability seen in individual profile comparisons. Selected profile–profile comparisons are shown in Figs. 11–15 but more attention should be given to the values in Table 7 where the differences are summarized. In the bottom (~30 km and below) of the lidar profiles, enhanced backscatter due to aerosols can sometimes make the temperatures systematically cold.

5.5.1. *TMF* (34°N, 118°W) *and MLO* (20°N, 156°W)

Due to large horizontal (~300 km) and vertical (~10 km) smearing it is not expected for MLS to catch the short-scale oscillations as seen in TMF temperature profiles. However, as shown in Fig. 11, some large-scale temperature oscillations in the mesosphere can be observed with MLS. Some 370 comparisons are found for the TMF location during 1992–1994 and the average bias shows that MLS is 2–4 K colder in the mesosphere except near 70 km where MLS is much colder by ~10 K. In the stratosphere MLS tracks TMF temperature very well except for a 1–4 K warm bias.

MLO measurements have slightly better sensitivity than TMF at the top and bottom of the altitude range (Leblanc and McDermid, 2001). As shown in Fig. 12, MLS is able to respond to some sharp temperature inversion events in

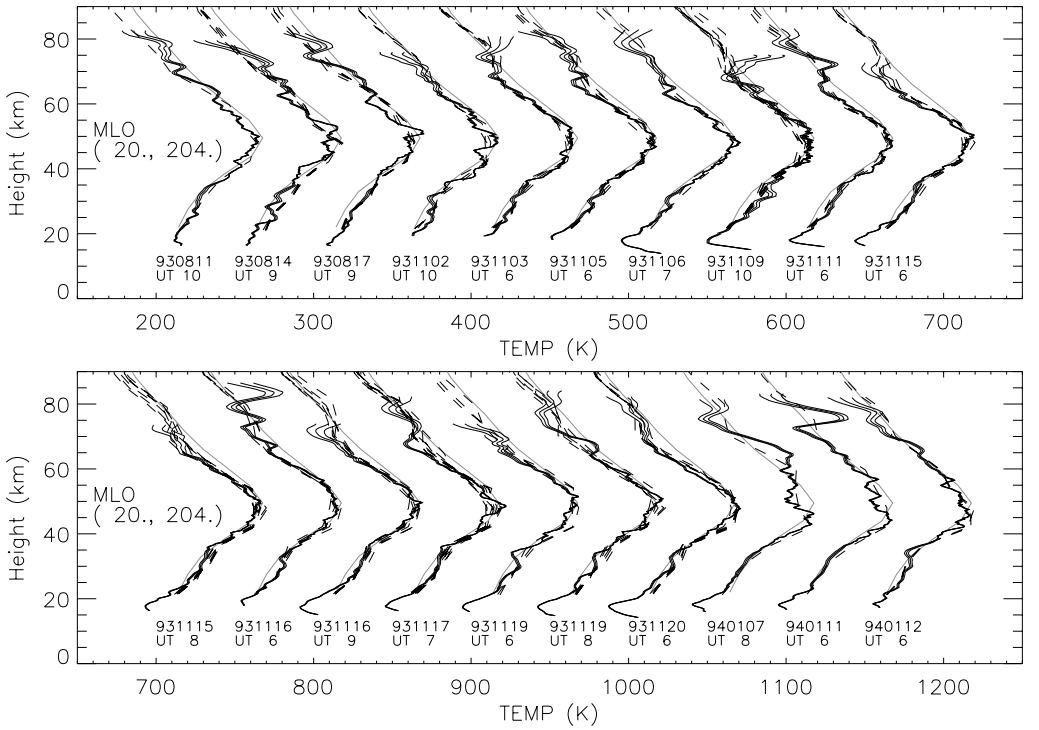

Fig. 12. Same as in Fig. 11 but for lidar measurements at Mauna Loa, Hawaii (20°N, 156°W).

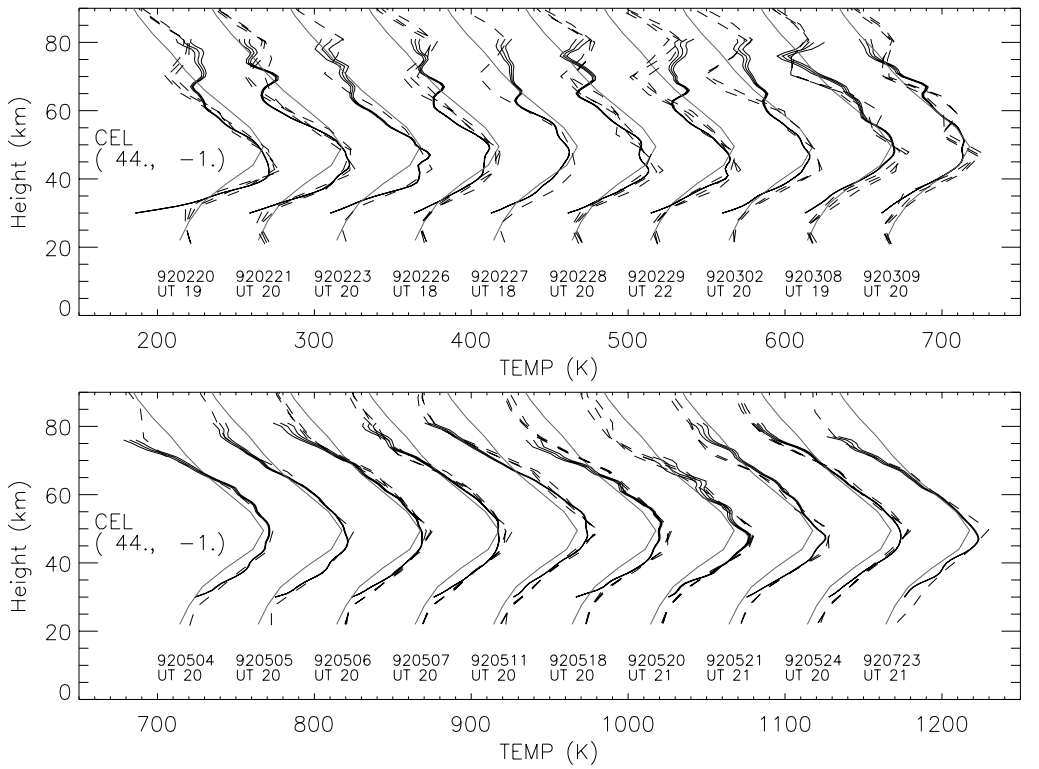

Fig. 13. Same as in Fig. 11 but for lidar measurements at CEL France (44°N, 1°W).

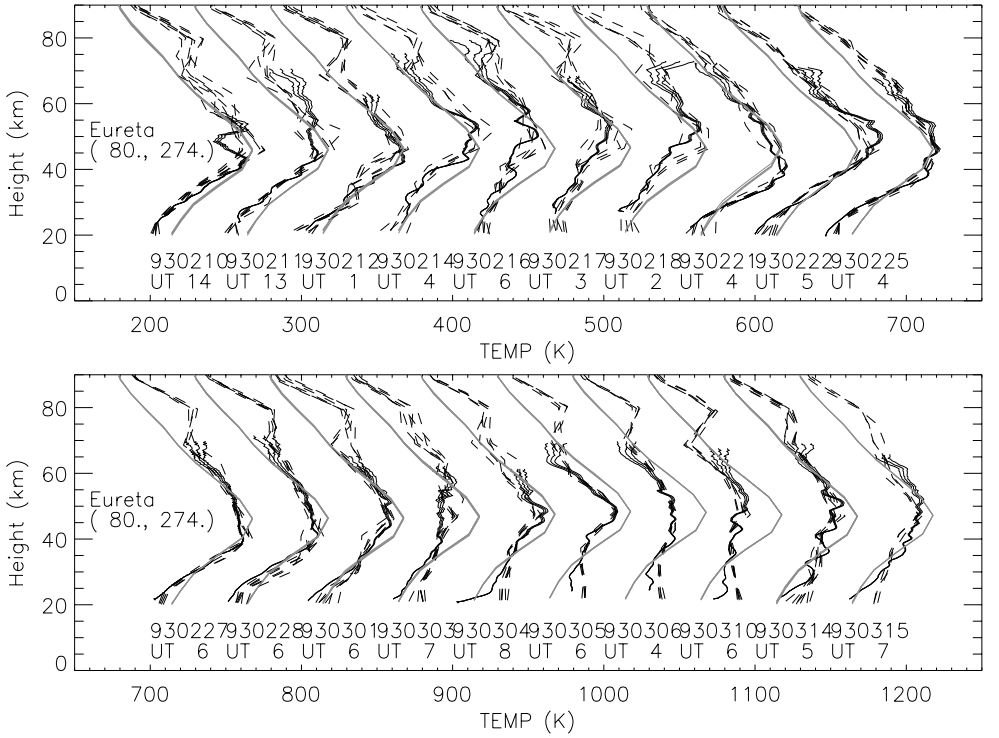

Fig. 14. Same as in Fig. 11 but for lidar measurements at Eureka (80°N, 86°W).

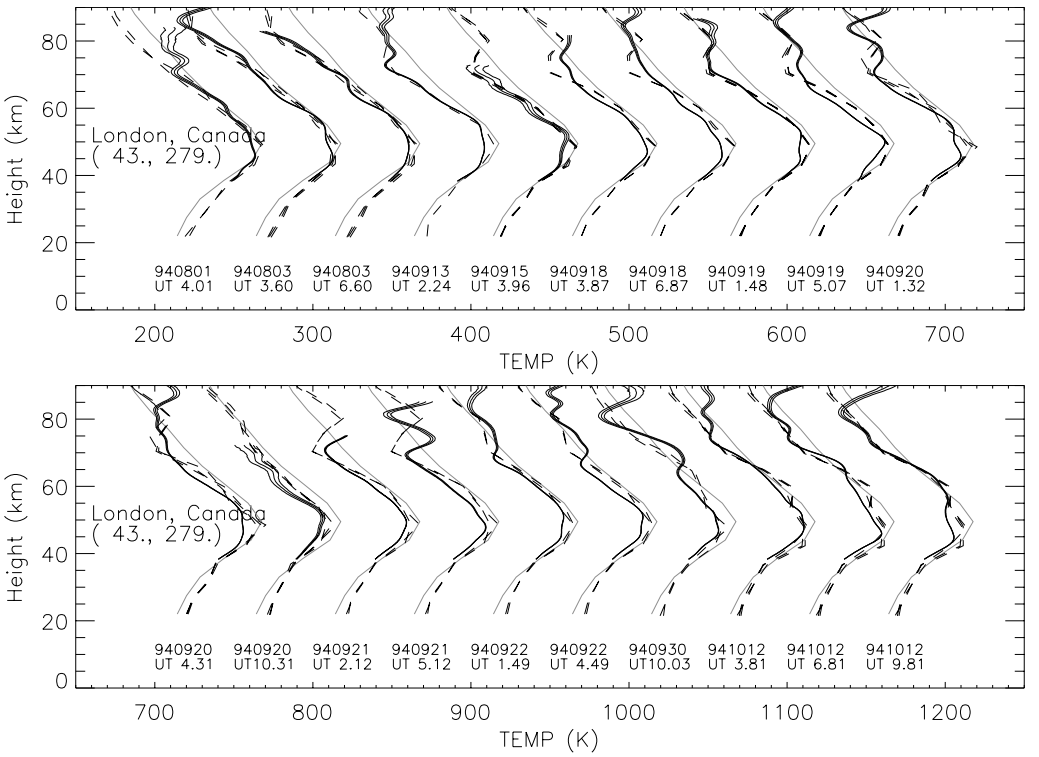

Fig. 15. Same as in Fig. 11 but for lidar measurements at London, Canada (43°N, 81°W).

Table 6
MLS and CSU monthly temperature (K) at Ft. Collin, CO (40.6°N, 105°W)

Height (km)	Jan	Feb	Mar	Apr	May	Jun	Jul	Aug	Sep	Oct	Nov	Dec
MLS												
80	216	215	214	185	185	—	185	196	200	204	206	217
85	204	199	200	184	178	—	176	185	190	194	194	203
90	189	186	187	182	173	—	172	177	181	183	183	187
CSU												
81	220	210	207	—	—	—	192	200	206	207	212	215
85	211	202	196	190	189	180	180	190	198	203	209	212
90	206	201	197	189	183	186	187	193	201	206	207	208

the mesosphere but the magnitude is much less than what the lidar measurements indicate. Apart from the differences due to small-scale variability, a general 2–3 K bias is found between 50 and 80 km before MLS exhibits a significant cold bias above 80 km. MLS temperature is ~10 K colder near ~85 km where MLO lidar observations have better sensitivity than TMF. The initial temperature at MLO is from the MSIS and often starts at an altitude around 90 km. Generally good agreement is found in the stratosphere except at ~43 km MLS is warmer by ~6 K.

5.5.2. *CEL* (44°N, 1°W) *and OHP* (44°N, 5°E)

Since CEL and OHP measurements are nightly temperatures made at close locations, we compare them together to MLS for better statistics. The duration of the lidar measurements often varies between 2 and 10 h depending on nighttime conditions, and CIRA'86 climatology is used to initialize the temperature at the top in the lidar retrievals (Hauchecorne and Chanin, 1980). MLS is warmer in general except at ~70 and ~53 km. Once again, the average bias at ~70 km indicates that MLS is ~8 K colder. At ~32 km the warm (5.4 K) bias may result from aerosol contamination to lidar signals at lower altitudes. It is often evident in the individual profile–profile comparisons that the aerosol problem produces cold lidar temperatures at the bottom of the profiles (Fig. 13).

5.5.3. *EUR* (80°N, 86°W)

EUR temperature profiles are nightly averages with 1.5 km altitude smoothing of the original 300 m resolution retrievals. This site location is very valuable for validating MLS retrievals under the extreme atmospheric conditions, such as the wintertime mesosphere (Duck et al., 2000). As shown in Fig. 14, large deviations from MLS a priori near 50 and 70 km are often seen at this location, and the ability of MLS tracking the lidar measurements is generally satisfactory in spite of small-scale features often missed by MLS. Near 70 km, again, it is a cold bias of 5 K, and the warm biases below 30 km are likely the result of aerosol influences.

5.5.4. *LON* (43°N, 81°W)

The lidar at London, Canada measures temperature with high precision in the upper mesosphere due mainly to its large power-aperture product (Sica et al., 1995). In this comparison we use 3-h averaged profiles with the top 8 km removed to neglect potential effects from the seed temperature (CIRA'86). As shown in Fig. 15. MLS often misses the temperature inversion near 90 km seen by the lidar, which is probably due to the poor sensitivity and vertical resolution associated with MLS, but agreement below 80 km becomes better (around ±6 K). Near 90 km, the MLS bias is worst (around −21 K), which is consistent with the comparisons with CIRA'86, HRDI, CRISTA1 and CSU lidar. It improves to −7 K near 85 km in line with the comparison to MLO measurements.

5.5.5. *CSU* (40.6°N, 105°W)

From the backscattering of the sodium layer, CSU lidar measures temperature and sodium density at 80–105 km (She et al., 1992). The best temperature sensitivity of CSU lidar is at altitudes between 85 and 95 km (with ~1 K error for hourly data). It degrades somewhat to ~4 and ~5 K near ~82 and ~105 km, respectively, as the sodium density drops.

In Table 6 are monthly averages of MLS nighttime temperature during 1991–1994 and CSU lidar 3-year nightly climatology (Yu and She, 1995). The CSU monthly means are based on observations from end of May 1991 to the beginning of 1994 with 4–5 nights a month. Through these monthly comparisons we may have an external verification about MLS temperature sensitivity and biases if the lidar measurements can be thought as the truth. First, MLS sensitivity may degrade slightly with height, showing annual peak-peak differences of 31, 26, 17 K at 80, 85, 90 km, respectively, when compared to 28, 31, 23 K observed with CSU lidar. Second, the mean bias increases with height as MLS sensitivity drops and shows that MLS temperature is generally colder in the upper mesosphere (Table 7), similar to the results in MLS-LON comparison.

Table 7
Summary of MLS-lidar differences

Height (km)	TMF		MLO		CEL/OHP		EUR		LON		CSU ΔT (K)
	No.	ΔT (K)	No.	ΔT (K)	No.	ΔT (K)	No.	ΔT (K)	No.	ΔT (K)	
90.7	—	—	—	—	—	—	—	—	36	−20.9	−16
85.3	—	—	12	−9.7	—	—	—	—	43	−6.7	−7
80.0	—	—	114	−0.3	178	5.5	—	—	48	0.2	1
74.7	172	−3.5	137	1.5	229	0.6	16	2.1	48	−5.4	—
69.3	343	−10.1	169	−3.0	245	−7.6	72	−5.0	56	−5.7	—
64.0	371	−2.6	169	0.5	246	0.3	125	3.0	56	4.2	—
58.7	371	−2.6	169	1.6	246	3.2	145	−0.5	56	5.6	—
53.3	371	−3.9	169	−2.1	246	−0.1	156	−0.5	56	1.1	—
48.0	371	2.7	169	2.4	246	5.2	161	5.4	56	6.4	—
42.7	371	1.5	169	5.8	246	3.4	161	−1.8	56	5.1	—
37.3	371	−0.2	169	1.7	246	0.9	161	−1.6	—	—	—
32.0	362	4.0	169	2.7	243	5.4	161	4.2	—	—	—
26.7	209	3.7	169	1.6	—	—	151	4.3	—	—	—
21.3	—	—	169	3.1	—	—	31	7.7	—	—	—

5.6. MLS-rocketsondes

Rocketsonde temperatures used in this comparison are the data made available by the rocketsonde investigators to the UARS project mostly during 1991–1995. Only rocketsonde temperatures measured with the falling sphere technique are used and they are limited to three locations: Wallops Island (38°N, 76°W), Andoya (69°N, 16°E), and Kiruna (68°N, 21°E). The typical rocketsonde temperature profiles range between 30 and 90 km with estimated precision of 1–2 K at 30–85 km and 2–8 K at 85–95 km. The accuracy of rocketsonde temperatures in the mesosphere is about 2% (Schmidlin et al., 1991; Lubken et al., 1994).

The criteria used for "coincident" measurements are same as in MLS-lidar comparisons. As shown in Fig. 16, there is good agreement between MLS and rocket measurements at Wallops Island at altitudes below ~70 km but the pictures is mixed between 70 and 90 km especially where there exists a sharp inversion structure. Table 8 summarizes the MLS-rocketsonde biases for the three locations with the best statistics at Wallops Island. Apart from the slight positive biases below 50 km, MLS is generally colder between 50 and 70 km, which might be related to the density uncertainty encountered by the rocketsondes at these altitudes (Schmidlin et al., 1991). This cold bias becomes worse at the Andoya and Kiruna sites (not shown here) as the temperature vertical gradients were greater than those at Wallops Islands. Above 85 km, the temperatures at Wallops Islands suggest the similar cold biases found in the MLS-lidar comparisons. However, warm biases are found in the Andoya and Kiruna comparisons at these altitudes with only several correlative observations.

Table 8
Summary of MLS-rocket differences

Ht. (km)	Wallops Is.		Andoya		Kiruna	
	No.	ΔT (K)	No.	ΔT (K)	No.	ΔT (K)
90.7	38	−14.1	18	35.1	—	—
85.3	44	−2.5	18	16.0	14	10.3
80.0	44	6.7	18	−0.5	14	0.9
74.7	46	0.7	18	−5.7	14	−5.4
69.3	46	−1.3	15	−4.3	14	−0.5
64.0	46	−8.0	15	−10.6	14	−11.2
58.7	46	−7.4	15	−22.5	14	−11.9
53.3	46	−4.6	15	−2.7	14	−6.8
48.0	46	2.9	15	2.1	14	7.6
42.7	40	2.3	15	3.0	14	8.9
37.3	36	1.3	15	3.6	14	4.2
32.0	15	−0.5	15	−1.7	14	0.4

6. Summary and conclusion

We have described a research algorithm for retrieving temperature and tangent pressure at altitudes of 20–90 km from UARS MLS 63 GHz O_2 radiances. The geomagnetic Zeeman effects on the O_2 emission are adequately modeled in the forward radiative transfer calculation so that the model can handle various geomagnetic conditions encountered by UARS MLS. A fast version of this model is developed based on the full forward model calculations, which is able to model limb radiances and weighting functions accurately and efficiently for practical retrieval uses. The radiance residuals are dominated by systematic error

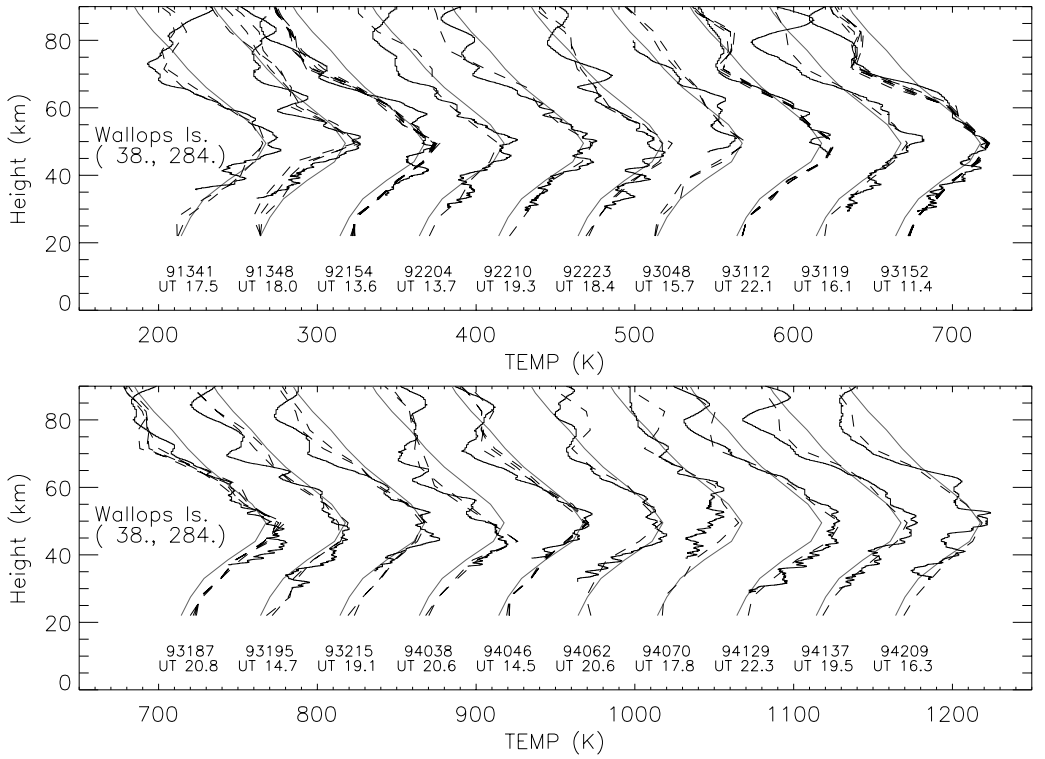

Fig. 16. Same as in Fig. 11 but for rocket measurements at Wallops Island (38°N, 76°W).

either in the instrument or in the forward model. There is a yaw-cycle dependence in the χ^2, indicating that the differences between the measured and modeled radiances are slightly larger near the yaw days when the instrument temperature is higher. Some remaining instrument error is likely to cause the yaw-cycle dependent χ^2. The radiance χ^2 after the retrieval may also come from large deviation between the truth and the linearization temperature profile, like the situations at high latitudes. Since this retrieval is based on the linearization on a single temperature profile, the larger temperature deviation would cause greater error in the linear retrieval.

Error analysis suggests that MLS is able to provide useful temperature measurements at 20–90 km although the instrument is not optimized for sounding the mesosphere. The new MLS temperature has an estimated precision of 1.5–4 K at 20–60 km, 6–8 K at 60–85 km, and $>$ 13 K above ~90 km. The sensitivity degradation in the upper mesosphere is also reflected in vertical resolution as a result of less independent radiance measurements (basically from channels 7–9). The instrument would produce better temperature sounding in the upper mesosphere if more narrow-bandwidth channels were added around the line center.

MLS temperature measurements are available for the period between September 1991 and June 1997, and the temperature retrieval has been compared to CIRA'86 climatology, satellite (ISAMS, HRDI, CRISTA1), and lidar/rocket observations to determine the measurement accuracy. General agreement with CIRA'86 climatology at 20–90 km is encouraging given that the MLS algorithm is based on the linearization on a single temperature profile. Comparisons with other correlative measurements show that MLS biases are generally less than 4 K at altitudes below ~65 km but increase to 10–15 K at ~90 km. A comparison to hydroxyl rotational temperatures near 87 km (not shown here) suggests a similar cold bias of ~10 K in MLS measurements at this altitude (Mulligan et al., 1995). Some of these biases are known to the shortcoming of the current MLS algorithm and will be reduced significantly in the future versions. Despite the existing biases, the MLS temperature has been found quite useful in studying global mesospheric phenomena. Studies showed that the new MLS temperature is able to capture many planetary-scale features such as the mesospheric inversion layer (Wu, 2000) and the quasi two-day ave (Azeem et al., 2001).

Acknowledgements

One of our authors, Mr. Zvi Shippony, made many key contributions to the forward model development while fighting for cancer in the past 2 years. Unfortunately, he passed

away before seeing his work published. We would like to dedicate this paper to Zvi for his persistent love and devotion to our research and education. This work was performed at Jet Propulsion Laboratory, California Institute of Technology, under contract with National Aeronautics and Space Administration, and sponsored by NASA. DLW would like to thank the UARS investigators for making correlative satellite, lidar and rocket data available to the project. CYS acknowledges NSF for providing funds to CSU under ATM 0003171.

References

Azeem, S.M.I., Palo, S.E., Wu, D.L., Froidevaux, L., 2001. Observations of the 2-day wave in UARS/MLS ozone measurements. Geophysical Research Letters 28, 3147–3150.

Barraclough, D., 1986. International geomagnetic reference field: the fourth generation. Physics of the Earth and Planetary Interiors 48, 279–292.

Barath, F.T., et al., 1993. The upper atmosphere research satellite microwave limb sounder instrument. Journal of Geophysical Research 98, 10,751–10,762.

Duck, T.J., Whiteway, J.A., Carswell, A.I., 2000. A detailed record of high Arctic middle atmospheric temperatures. Journal of Geophysical Research 105, 22,909–22,918.

Dudhia, A., Livesey, N., 1996. Validation of ISAMS temperature. Journal of Geophysical Research 101, 9795.

Fishbein, E., et al., 1996. Validation of UARS Microwave Limb Sounder temperature and pressure measurements. Journal of Geophysical Research 101, 9983–10016.

Fleming, E.S., et al., 1990. Zonal mean temperature, pressure, zonal wind, and geopotential height as function of latitude. Advances in Space Research 10, 11–59.

Hartmann, G.K., et al., 1996. Zeeman splitting of the 61 Gigahertz Oxygen (O_2) line in the mesosphere. Geophysical Research Letters 23, 2329–2332.

Hauchecorne, A., Chanin, M.L., 1980. Density and temperature profiles obtained by lidar between 35 and 70 km. Geophysical Research Letters 8, 565–568 (1980).

Hedin, A.E., 1991. Extension of the MSIS thermosphere model into the middle and lower atmosphere. Journal of Geophysical Research 96 (A2), 1159–1172.

Jarnot, R.F., Cofield, R.E., Waters, J.W., Flower, D.A., Peckham, G.E., 1996. Calibration of the microwave limb sounder on the upper atmosphere research satellite. Journal of Geophysical Research 101, 9957–9982.

Leblanc, T., McDermid, I.S., 2001. Quasi-biennial oscillation signatures in ozone and temperature observed by lidar at Mauna Loa, Hawaii (19.5 degrees N, 155.6 degrees W). Journal Geophysical Research 106, 14,869–14,874.

Lenoir, W., 1967. Propagation of partially polarized waves in a slightly anisotropic medium. Journal of Applied Physics 38, 5283–5290.

Lenoir, W., 1968. Microwave spectrum of molecular oxygen in the mesosphere. Journal of Geophysical Research 73, 361–376.

Liebe, H.J., 1989. MPM-An atmospheric millimeter-wave propagation model. International Journal of Infrared and Millimeter Waves 10, 631–650.

Livesey, N., 1995. Ph.D. dissertation, University of Oxford, UK, pp. 238.

Livesey, N. et al., 2002. The UARS Microwave Limb Sounder version 5 dataset: theory, characterization and validation. Journal of Geophysical Research, in press.

Lubken, F.-J., et al., 1994. Intercomparison of density and temperature profiles obtained by lidar ionization gauges, falling spheres, datasondes and radiosondes during the DYANA campaign. Journal of Atmospheric and Terrestrial Physics 56, 1969–1984.

Mulligan, F.J., Horgan, D.F., Galligan, J.G., Griffin, E.M., 1995. Mesopause temperatures and integrated band brightnesses calculated from airglow OH emissions recorded at Maynooth ($53.2°N, 6.4°W$) during 1993. Journal of Atmospheric and Terrestrial Physics 57, 1623–1637.

Oberheide, J., Hagan, M.E., Ward, W.E., Riese, M., Offermann, D., 2000. Modeling the diurnal tide for the Cryogenic Infrared Spectrometers and Telescopes for the Atmosphere (CRISTA) 1 time period. Journal of Geophysical Research-Space 105, 24,917–24,929.

Ortland, D.A., Hays, P.B., Skinner, W.R., Yee, J.H., 1998. Remote sensing of mesospheric temperature and O-2(1-Sigma) band volume emission rates with the high-resolution Doppler imager. Journal of Geophysical Research 103 (D2), 1821–1835.

Pardo, J.R., Pagani, L., Gerin, M., Prigent, C., 1995. Evidence of the Zeeman splitting in the $2_1 \rightarrow 0_1$ rotational transition of the atmospheric $^{16}O^{18}O$ molecule from ground-based measurements. Journal of Quantitative Spectroscopy & Radiative Transfer 54, 931–943.

Riese, M., et al., 1999. CRISTA data processing and atmospheric temperature and trace gas retrieval. Journal of Geophysical Research 104, 16,349–16,367.

Rodgers, C.D., 1976. Retrieval of atmospheric temperature and composition from remote measurements of thermal radiation. Reviews of Geophysics and Space Physics 14 (4), 609–624.

Rosenkranz, P.W., Staelin, D.H., 1988. Polarized thermal microwave emission from oxygen in the mesosphere. Radio Science 23, 721–729.

Schmidlin, F.J., Lee, H.S., Michel, W., 1991. The inflatable sphere: a technique for the accurate measurement of middle atmosphere temperatures. Journal of Geophysical Research 96, 22,673–22,682.

She, C.Y., Yu, J.R., Latifi, H., Bills, R.E., 1992. High-spectral-resolution lidar for mesospheric sodium temperature measurements. Applied Optics 31, 2095–2106.

Sica, R.J., et al., 1995. Lidar measurements taken with a large-aperture liquid mirror. 1. Rayleight-scatter system. Applied Optics 34, 6925–6936.

Stogryn, A., 1989a. The magnetic field dependence of brightness temperatures at frequencies near the O_2 microwave absorption lines. IEEE Transactions on Geoscience and Remote Sensing 27, 279–289.

Stogryn, A., 1989b. Mesospheric temperature sounding with microwave radiometers. IEEE Transactions on Geoscience and Remote Sensing 27, 332–338.

von Engeln, A., Langen, J., Wehr, T., Buhler, S., Kunzi, K., 1998. Retrieval of upper stratospheric and mesospheric temperature profiles from millimeter-wave atmospheric sounder data. Journal of Geophysical Research 103, 31,735–31,748.

Waters, J.W., 1973. Ground-based measurement of millimeter-wavelength emission by upper stratospheric O_2. Nature 242, 506–508.

Waters, J.W., 1993. In: Janssen, M.A. (Ed.), Atmospheric Remote Sensing Microwave Radiometry. Wiley, New York, pp. 383–496. Chap.8.

Wu, D.L., 2000. Mesospheric temperature inversion layers as observed by UARS MLS and ISAMS. Recent Research and Development in Geophysics, Research Signpost, March, pp. 37–44.

Wu, D.L., Waters, J.W., 1996. Satellite observations of atmospheric variances: a possible indication of gravity waves. Geophysical Research Letters 23, 3631–3634.

Yu, J.R., She, C.Y., 1995. Climatology of a midlatitude mesopause region observed by a lidar at Fort Collins, Colorado (40.6°N, 105°W). Journal of Geophysical Research 100, 7441–7452.